### Title

Alzheimer's disease 5xFAD mice with beta-amyloid plaques have increased alpha4beta2*nicotinic acetylcholinergic receptors




### Authors

Liang, Christopher
Nguyen, An
Syed, Amina
et al.



### Publication Date

2022

Peer reviewed

Received: 18 October 2022 | Revised: 31 January 2023 | Accepted: 2 February 2023

DOI: 10.1002/syn.22265

SYNAPSE WILEY

RESEARCH ARTICLE

# Abnormal [$^{18}$F]NIFENE binding in transgenic 5xFAD mouse model of Alzheimer's disease: In vivo PET/CT imaging studies of $\alpha4\beta2^*$ nicotinic acetylcholinergic receptors and in vitro correlations with A$\beta$ plaques

**Christopher Liang** | **Grace A. Nguyen** | **Tram B. Danh** | **Anoopraj K. Sandhu** | **Lusine L. Melkonyan** | **Amina U. Syed** | **Jogeshwar Mukherjee**

Preclinical Imaging, Department of Radiological Sciences, University of California-Irvine, Irvine, California, USA

**Correspondence**
Jogeshwar Mukherjee, Preclinical Imaging, B140 Medical Sciences, Department of Radiological Sciences, University of California-Irvine, Irvine, CA 926976-5000, USA.
Email: j.mukherjee@uci.edu

Presented in part at the Annual Society of Nuclear Medicine, June 13–16, 2022.

**Funding information**
National Institutes of Health, Grant/Award Number: NIH AG029479

## Abstract

Since cholinergic dysfunction has been implicated in Alzheimer's disease (AD), the effects of A$\beta$ plaques on nicotinic acetylcholine receptors (nAChRs) $\alpha4\beta2^*$ subtype were studied using the transgenic 5xFAD mouse model of AD. Using the PET radiotracer [$^{18}$F]nifene for $\alpha4\beta2^*$ nAChRs, in vitro autoradiography and in vivo PET/CT studies in 5xFAD mice were carried out and compared with wild-type (C57BL/6) mice. Ratios of [$^{18}$F]nifene binding in brain regions versus cerebellum (CB) in 5xFAD mice brains were for thalamus (TH) = 17, hippocampus-subiculum = 7, frontal cortex (FC) = 5.5, and striatum = 4.7. [$^{125}$I]IBETA and immunohistochemistry (IHC) in 5xFAD brain slices confirmed A$\beta$ plaques. Nicotine and acetylcholine displaced [$^{18}$F]nifene in 5xFAD mice ($IC_{50}$ nicotine = 31–73 nM; ACh = 38–83 nM) and C57BL/6 ($IC_{50}$ nicotine = 16–18 nM; ACh = 34–55 nM). Average [$^{18}$F]nifene SUVR (CB as reference) in 5xFAD mice was significantly higher in FC = 3.04 compared to C57BL/6 mice FC = 1.92 ($p$ = .001), whereas TH difference between 5xFAD mice (SUVR = 2.58) and C57BL/6 mice (SUVR = 2.38) was not significant. Nicotine-induced dissociation half life ($t_{1/2}$) of [$^{18}$F]nifene for TH were 37 min for 5xFAD mice and 26 min for C57BL/6 mice. Dissociation half life for FC in C57BL/6 mice was 77 min , while no dissociation of [$^{18}$F]nifene occurred in the medial prefrontal cortex (mFC) of 5xFAD mice. Coregistration of [$^{18}$F]nifene PET with MR suggested that the mPFC, and anterior cingulate (AC) regions exhibited high uptake in 5xFAD mice compared to C57BL/6 mice. Ex vivo [$^{18}$F]nifene and in vitro [$^{125}$I]IBETA A$\beta$ plaque autoradiography after in vivo PET/CT scan of 5xFAD mouse brain were moderately correlated ($r^2$ = 0.68). In conclusion, 5xFAD mice showed increased non-displaceable [$^{18}$F]nifene binding in mPFC.

**KEYWORDS**
[$^{18}$F]Nifene, [$^{125}$I]IBETA, [$^{18}$F]FEPPA, PET/CT, 5xFAD transgenic mice, Alzheimer's disease

  

## 1 | INTRODUCTION

Alzheimer's disease (AD) in humans involves several distinct pathologies and includes accumulation of extracellular insoluble $\beta$-amyloid plaques (A$\beta$ plaques), intercellular hyperphosphorylated tau protein resulting in neurofibrillary tangles (NFT), inflammation, progressive atrophy, synapse loss, and cell death in neurons (Braak et al., 2011). Memory and cognition deficits occur concurrently with the cell loss in mild cognitive impairment (MCI), and these eventually degrade into dementia in AD. There is an immediate need for understanding the neurobiological basis of the various pathologies found in AD in order to develop suitable treatment strategies (Desmarais & Gauthier, 2010; Salloway et al., 2014; Samra et al., 2018).

Cholinergic pathway deficits in AD have been associated with cognitive impairment. The $\alpha4\beta2^*$ nicotinic acetylcholine receptor (nAChR, $\alpha4\beta2^*$ includes subtypes $\alpha2\beta2$, $\alpha3\beta2$, and $\alpha4\beta2$) is involved in cognitive functions such as attention, learning, and memory. Deficiency in cholinergic innervation in the cerebral cortex and hippocampus was observed (Coyle et al., 1983; Marutle et al., 1999), and $\alpha4\beta2^*$ nAChRs constitute a major subtype lost in postmortem AD brains (Nordberg, 1994; Okada et al., 2013; Sultzer et al., 2022). Treatment with acetylcholinergic inhibitors (AChEI) has been found to slow the decline in AD (Zuin et al., 2022). Direct interactions of A$\beta$ with nAChRs may also contribute to AD pathology (Lombardo & Maskos, 2015). Thus, there is a need to examine the potential in vivo role of A$\beta$ plaques on $\alpha4\beta2^*$ nAChR.

Transgenic mice models allow the study of specific pathology such as A$\beta$ plaques in AD (Webster et al., 2014). Positron emission tomography (PET) imaging studies, including the metabolic probe ([$^{18}$F]FDG), have been used in different transgenic models of AD in an effort to understand biochemical abnormalities (Coleman et al., 2017; Jullienne et al., 2022; Luo et al., 2012). The Swedish mutation of amyloid precursor protein (APP) in the transgenic Tg2576 mice causing deposition of A$\beta$ in the brains has been well described (Kawarabayashi et al., 2001). In contrast, the 5xFAD transgenic mice overexpress mutant human APP with the Swedish (K670N, M671L), Florida (I716V), and London (V717I) familial AD (FAD) mutations and human presenilin 1 (PS1) harboring two FAD mutations, M146L and L286V (Oakley et al., 2006). The 5xFAD mice generate A$\beta$-42 almost exclusively, rapidly accumulating massive cerebral levels of A$\beta$-42, followed by accumulation of A$\beta$ plaques. At the age of 18 months, the mice develop extensive A$\beta$ deposits and serve as good models of advanced human AD (Forner et al., 2021; Oblak et al., 2021). PET imaging studies in the 5xFAD transgenic mice have been carried out using various PET probes including A$\beta$ plaque imaging [$^{18}$F]florbetaben (Boulter et al., 2021; Jullienne et al., 2022). Our recent findings using brain slices in vitro autoradiography and in vivo PET confirmed A$\beta$ plaque accumulation in 5xFAD mice using the imaging agent [$^{124/125}$I]IBETA (Nguyen et al., 2022). Human AD brain slices were also successfully labeled with [$^{124/125}$I]IBETA suggesting similarity of binding sites in the 5xFAD mice and human A$\beta$ plaques (Nguyen et al., 2022). Thus, 5xFAD mice would be a good transgenic mouse model to study the effects of A$\beta$ plaques on $\alpha4\beta2^*$ nAChR.

Several efforts using PET imaging of $\alpha4\beta2^*$ nAChR in human AD have been made (Sabri et al., 2018; Sultzer et al., 2017). A reduction of $\alpha4\beta2^*$ nAChR was observed in certain brain regions, which was consistent with postmortem finding in AD brains (Colloby et al., 2010; Mitsis et al., 2009). Using [$^{18}$F]nifene for imaging $\alpha4\beta2^*$ nAChR, we have found a reduction in postmortem human AD subjects compared to controls (Mukherjee et al., 2021). Biological properties of [$^{18}$F]nifene reported in rodents (Bieszczad et al., 2012; Campoy et al., 2021; Kant et al., 2011), monkeys (Hillmer et al., 2011; Pichika et al., 2006), and humans (Mukherjee et al., 2018) suggest suitability of [$^{18}$F]nifene to study transgenic 5xFAD model for understanding the role of A$\beta$ plaques on the $\alpha4\beta2^*$ nAChR in human AD.

Regional brain distribution of high A$\beta$ plaque accumulation, determined using fluorescence imaging and anti-A$\beta$ immunohistochemistry have been reported (Forner et al., 2021; Oblak et al., 2021). Radioligand autoradiography in the 5xFAD brains confirms A$\beta$ plaques in cortex, including anterior cingulate, frontal cortex, hippocampus, lateral septal nuclei, and thalamic brain regions (Nguyen et al., 2022). Normal mouse brain distribution of [$^{18}$F]nifene binding includes cortex, including anterior cingulate, frontal cortex, thalamus, subiculum (with low levels in the hippocampus, mostly in the dentate gyrus), and striatum with very low levels in the cerebellum (Campoy et al., 2021) Thus, there are several overlapping mouse brain regions where A$\beta$ plaques and $\alpha4\beta2^*$ nAChRs are localized.

Figure 1A shows elements of the cholinergic neuron with potential interaction of the neurotransmitter acetylcholine (Ach), nicotine, and [$^{18}$F]nifene at the receptor site as well as acetylcholinesterase (AChE)-catalyzed hydrolysis of ACh to choline. Figure 1B shows the accumulation of A$\beta$ plaques in overlapping brain regions which are likely to interrupt binding of ACh, interact with $\alpha4\beta2^*$ nAChRs, affect presynaptic choline, or block this neurotransmission. Inhibitors (AChEI) for AChE have been used to stop AChE from hydrolyzing ACh in attempts to increase the amount of ACh to improve cholinergic deficit in AD (Easwaramoorthy et al., 2007). However, use of AChEI in the treatment of AD has been hampered because of their poor efficacy (Marucci et al., 2021). The 5xFAD mice expressing A$\beta$ plaques are an excellent model to examine potential alterations in $\alpha4\beta2^*$ nAChRs using in vivo PET/CT studies. They provide ages that resemble pre-AD A$\beta$ pathology, early AD pathology, and late-stage AD pathology (Forner et al., 2021; Oblak et al., 2021). Because of the small size of the mouse brain, in vivo PET/CT imaging is more reliable for larger regions such as thalamus, cortex, and cerebellum. Other smaller brain regions with A$\beta$ plaques and [$^{18}$F]nifene binding will require a careful in vivo–ex vivo imaging paradigm, as reported before (Bieszczad et al., 2012).

In order to assess the in vivo effects of A$\beta$ plaque pathology on $\alpha4\beta2^*$ nAChRs, we report in vivo PET/CT studies of [$^{18}$F]nifene in 12- to 18-month-old 5xFAD mice, which have been shown to express A$\beta$ plaques resembling advanced human AD. Studies include (1) in vitro binding studies in C57BL/6 and 5xFAD mice; (2) nicotine and acetylcholine competition in vitro; (3) in vivo PET/CT imaging studies in C57BL/6 and 5xFAD mice; (4) nicotine challenge in C57BL/6 and 5xFAD mice using [$^{18}$F]nifene PET/CT imaging studies; (5) A$\beta$ plaques immunohistochemical staining and

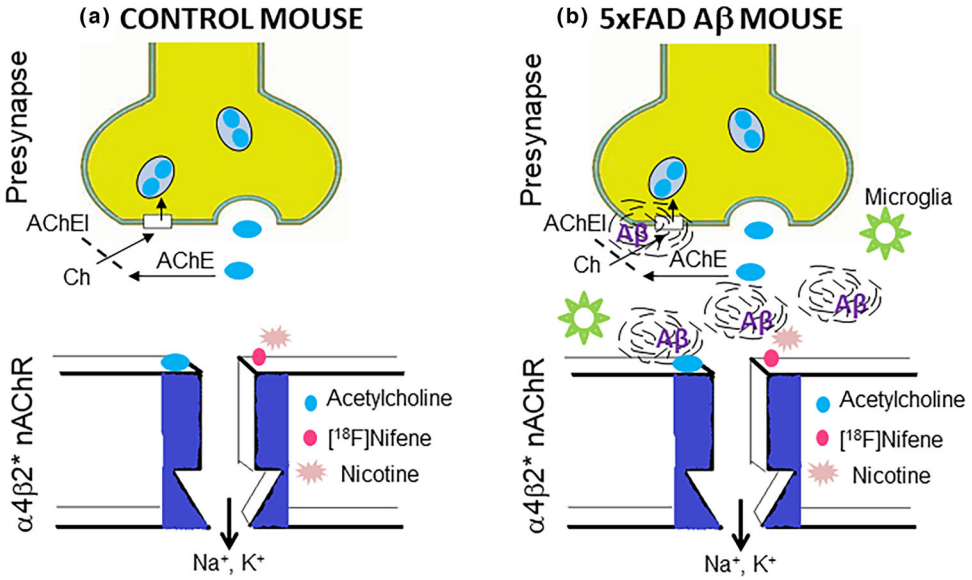


**FIGURE 1** Schematic of $\alpha4\beta2^*$ nAChRs in 5xFAD AD mice: (A) Schematic showing synaptic junction of $\alpha4\beta2^*$ nAChR in normal mouse. (B) In 5xFAD transgenic mouse, Aβ plaques and microglia present in the synapses which may interact and/or interrupt [$^{18}$F]nifene, acetylcholine, and nicotine binding. AChE, acetylcholinesterase; AChEI, acetylcholinesterase inhibitors; AD, Alzheimer's disease; Ch, choline; nAChR, nicotinic acetylcholine receptor.

autoradiography using [$^{125}$I]IBETA (Nguyen et al., 2022) and correlation with [$^{18}$F]nifene binding; (6) evaluation of [$^{18}$F]FEPPA in vitro binding to translocator protein (TSPO; Vignal et al., 2018), a microglia biomarker in 5xFAD brain slices.

## 2 | MATERIALS AND METHODS

### 2.1 | General methods

All chemicals and solvents were purchased from Aldrich Chemicals Inc. and Fisher Scientific Inc. Deionized water was acquired from Millipore Milli-Q Water Purification System. Fluorine-18 fluoride in oxygen-18 enriched water was purchased from PETNET, Inc. Iodine-125 was purchased from American Radiolabeled Chemicals, Inc. Fluorine-18 and iodine-125 radioactivity were counted in a Capintec CRC-15R dose calibrator, while low level counting was carried out in a Capintec Caprac-R well-counter. All solvents used were provided by Fisher Scientific. Gilson high-performance liquid chromatography (HPLC) was used for the semi-preparative reverse-phase column chromatography with UV detector set at dual wavelengths of 254 and 280 nm as well as a radioactivity detector. A semi-preparative HPLC column 100 × 250 mm 10 micron Econosil C18 reverse-phase was used. Analytical thin-layer chromatography (TLC) was used to monitor reactions (Baker-flex, Phillipsburg, NJ, USA). RadioTLC were scanned on an AR-2000 imaging scanner (Eckart & Ziegler, Berlin, Germany). Electrospray mass spectra were obtained from a Model 7250 mass spectrometer (Micromass LCT). Proton NMR spectra were recorded on a Bruker OM EGA 500-MHz spectrometer. Mice brain slices were prepared at 10–40 $\mu$m thick using the Leica 1850 cryotome. In vitro or ex vivo labeled brain sections were exposed to phosphor films (Perkin Elmer Multisensitive, Medium MS) and read using the Cyclone Phosphor Imaging System (Packard Instruments). Analysis of in vitro or ex vivo autoradiographs was done using the Optiquant acquisition and analysis software.

### 2.2 | Animals

All animal studies were approved by the Institutional Animal Health Care and Use Committee of University of California-Irvine. Transgenic 5xFAD mice (B6SJL-Tg(APPSwFlLon, PSEN1*M146L*L286V)6799Vas/Mmjax) were obtained from Jackson Laboratory (MMRRC stock#34840) and in-house resources, female ($n$ = 14) and male ($n$ = 6), weight range = 20–30 g, and age range of 12–18 months. Control mice (C57BL/6), female ($n$ = 6) and male ($n$ = 6), weight range = 30–46 g, and age range of 12–18 months from Jackson Laboratory, were used. Mice were housed under controlled temperatures of 22 ± 1°C, in a 12-h light–dark cycle, at 6:00 a.m., with water and food chow ad libitum. All animals recovered from the isoflurane anesthesia required for the PET/CT imaging procedures. None of the mice exhibited any signs of hind limb paralysis as was observed with the Hualpha-Syn (A53T) Parkinson's disease mouse model of α-synucleinopathy (Mondal et al., 2021).

## 2.3 | Radiopharmaceuticals

### 2.3.1 | [$^{18}$F]Nifene

The radiosynthesis of [$^{18}$F]nifene was performed using nucleophilic displacement of the nitro group in *N*-BOC-nitronifene precursor (prepared in-house, Pichika et al., 2006) by [$^{18}$F]fluoride in an automated synthesizer followed by deprotection using previously described procedures (Campoy et al., 2021; Pichika et al., 2006). The final formulation of [$^{18}$F]nifene was carried out using sterile saline (0.9% NaCl injection, United States Pharmacopeia) in a dose vial for use in the PET studies. Radiochemical purity of [$^{18}$F]Nifene was >98%, and chemical purity was found to be >95% with a measured molar activity >70 GBq/$\mu$mol (>2 Ci/$\mu$mol) at the end of synthesis.

### 2.3.2 | [$^{125}$I]IBETA

[$^{125}$I]IBETA is a new radiotracer for imaging A$\beta$ plaques (Nguyen et al., 2022; Ono et al., 2013). [$^{125}$I]IBETA and [$^{124}$I]IBETA exhibited selective binding to both 5xFAD and human AD brain A$\beta$ plaques and were displaced with known A$\beta$ plaques binding agents, flotaza and TAZA (Kaur et al., 2021; Pan et al., 2016). The radiosynthesis of [$^{125}$I]IBETA was performed using sodium [$^{125}$I]iodide under electrophilic destannylation reaction conditions (Nguyen et al., 2022). The final formulation of [$^{125}$I]IBETA was in alcohol. Radiochemical purity of [$^{125}$I]IBETA was >95% with a measured molar activity >500 GBq/$\mu$mol (>13 Ci/$\mu$mol).

### 2.3.3 | [$^{18}$F]FEPPA

The single-step radiosynthesis of [$^{18}$F]FEPPA was performed using nucleophilic displacement of the tosylate precursor (*N*-acetyl-*N*-(2-tosylethoxybenzyl)-2-phenoxy-5-pyridinamine, from ABX, Inc.) by [$^{18}$F]fluoride using reported methods (Vignal et al., 2018). [$^{18}$F]FEPPA was purified by reverse-phase HPLC, and the final formulation of [$^{18}$F]FEPPA was carried out using 10% alcohol in sterile saline (0.9% NaCl injection, United States Pharmacopeia) in a dose vial for use in the in vitro studies. Radiochemical purity of [$^{18}$F]FEPPA was >95%, and chemical purity was found to be >95% with a measured molar activity >70 GBq/$\mu$mol (>2 Ci/$\mu$mol) at the end of synthesis.

## 2.4 | In vitro mice brain [$^{18}$F]Nifene studies

Mice (5xFAD and controls) were decapitated, and the brain was rapidly removed and stored at -80°C. Horizontal sections (10 $\mu$m thick) containing the cortex, striatum, thalamus, hippocampus, subiculum, and cerebellum were prepared using LEICA CM 1850 cryotome at −20°C and stored at −80°C until use. For binding studies, slides were thawed for approximately 15 min at ambient temperature and were subsequently pre-incubated for 10 min at ambient temperature in buffer (120 mmol/L Tris HCl containing 5 mmol/L NaCl, 5 mmol/L KCl, 2.5 mmol/L $CaCl_2$, 1 mmol/L $MgCl_2$, pH 7.4). The preincubation buffer was then discarded. Subsequently, the slices were treated with incubation buffer containing [$^{18}$F]nifene (148 kBq/mL) at 20–22°C for 60 min. Nonspecific binding was measured in the presence of 300 $\mu$mol of nicotine. After incubation, slides were washed twice (2 min each) with ice-cold incubation buffer, followed by a quick rinse in cold (0–5°C) deionized water. The dried slides were apposed to phosphor screens and read by the Cyclone Phosphor Imaging System (Packard Instruments Co.). The amount of bound [$^{18}$F]nifene in the autoradiograms was evaluated in various brain regions (as digital lights units [DLU]/mm$^2$) using the OptiQuant acquisition and analysis program (Packard Instruments Co.) as previously reported (Campoy et al., 2021).

The effect of nicotine in vitro binding of [$^{18}$F]nifene in 5xFAD and control mice was evaluated. Competitive binding assay with different concentrations of nicotine (1 nM to 10 $\mu$M) was carried out using horizontal brain slices under the conditions described above. Changes in [$^{18}$F]nifene binding were evaluated in various regions in the brain sections of 5xFAD and control mice. Effect of acetylcholine was evaluated in mice brain sections in the presence of 200 $\mu$M physostigmine as previously reported in rat brain slices (Easwaramoorthy et al., 2007). Competitive binding assay with different concentrations of acetylcholine (1 nM to 10 $\mu$M) was carried out using the conditions described above. Effects of acetylcholine on [$^{18}$F]nifene binding were evaluated in the autoradiograms in various regions in the brain sections of 5xFAD and control mice. Data were analyzed using the following procedure: (1) the nonspecific binding of [$^{18}$F]nifene was subtracted for all samples; (2) the specific binding was normalized to 100% (no competitive ligand), and (3) the binding isotherms were fit to the Hill equation (KELL BioSoft software [v 6], Cambridge, U.K.) to provide inhibitor concentration ($IC_{50}$), which is the inflection point of the isotherm where 50% of the [$^{18}$F]nifene binding to nicotinic receptor was displaced by nicotine or acetylcholine.

## 2.5 | [$^{125}$I]IBETA 5xFAD mice brain in vitro autoradiography for A$\beta$ plaques

In order to assess A$\beta$ plaque load in the 5xFAD mice brain slices, in vitro studies using [$^{125}$I]IBETA were carried out using our previously described procedures for imaging A$\beta$ plaques in human postmortem brains (Nguyen et al., 2022). Mice brain slices, 5xFAD, and control mice (10 $\mu$m thick) treated with [$^{125}$I]IBETA in 40% ethanol phosphate buffered saline (PBS) buffer pH 7.4 (60 mL; 1.5 kBq/mL) were incubated at 25°C for 1.25 h. Nonspecific binding was measured in the presence of flotaza (Kaur et al., 2021). The slices were then washed with cold PBS buffer, 90% ethanolic PBS buffer twice, PBS buffer, and cold water (Nguyen et al., 2022). The brain sections were air dried, exposed overnight on a phosphor film, and then read on the Cyclone Storage Phosphor System. The amount of bound [$^{125}$I]IBETA in the autoradiograms was evaluated in various brain regions (as DLU/mm$^2$) using the OptiQuant acquisition and analysis program (Packard Instruments Co.). Binding of [$^{125}$I]IBETA was compared with [$^{18}$F]nifene and anti-A$\beta$ immunostained adjacent 5xFAD brain slices.

## 2.6 | PET/CT imaging 5xFAD mice [$^{18}$F]Nifene

The Inveon PET and MM CT scanners were placed in the "docked mode" for combined PET/CT experiments. PET data were reconstructed as 128 × 128 × 159 matrices with a transaxial pixel of 0.776 mm and slice thickness of 0.796 mm using an OSEM3D algorithm (two OSEM iterations, 18 MAP iterations (Constantinescu & Mukherjee, 2009). PET images were corrected for random coincidences, attenuation, and scatter. All images were calibrated in units of Bq/cm$^3$ by scanning a Ge-68 cylinder (6 cm diameter) with known activity and reconstructing the acquired image with parameters identical to those of [$^{18}$F]nifene images. The CT images were spatially transformed to match the reconstructed PET images. The CT projections were acquired with the detector-source assembly rotating over 360° and 720 rotation steps. A projection bin factor of 2 was used in order to increase the signal-to-noise ratio in the images. The CT images were reconstructed using cone-beam reconstruction with a Shepp filter with cutoff at Nyquist frequency and a binning factor of 2 resulting in an image matrix of 512 × 512 × 1008 and a voxel size of 0.052 mm.

Male and female transgenic 5xFAD mice and control C57BL/6 mice male and female were used in the study. All mice were fasted for approximately 18 h prior to the imaging study. The fasting minimizes fluctuating blood sugar levels, which may cause variations in receptor studies. In addition, fasting minimizes artifacts in the PET/CT imaging due to contents in the gastrointestinal tracts. No undue stress was observed in the mice due to fasting. All mice were injected [$^{18}$F]Nifene intraperitoneally in normal saline (7.4 ± 0.7 MBq in 0.05–0.1 mL sterile saline) under 2% isoflurane (St. Joseph, MO, USA). For static scans, mice were awake after [$^{18}$F]nifene injections and free to move in their cages.

### 2.6.1 | Dynamic scans

Injected mice were placed in the supine position in a mouse holder and anesthetized with 2% isoflurane for whole-body PET/CT imaging. Dynamic PET scans were acquired for 2 h after [$^{18}$F]nifene injections (Constantinescu et al., 2013). Before the PET scan, the scanner bed was moved to the CT for a 7.5-min-long CT scan, which was used for attenuation correction and anatomical delineation of PET images. The Inveon multimodality scanner was used for all combined PET/CT experiments.

### 2.6.2 | Static scans

Injected mice were placed in the supine position in a mouse holder and anesthetized with 2% isoflurane for whole-body PET/CT imaging. A 30 min-long PET scan was acquired 40 min after [$^{18}$F]nifene injections preceded by a 7.5-min-long CT scan before the PET scan for attenuation correction and anatomical delineation of PET images. The Inveon multimodality scanner was used for all combined PET/CT experiments.

## 2.7 | In Vivo nicotine effects 5xFAD mice [$^{18}$F]Nifene PET/CT

To assess effects of nicotine treatment in vivo, 5xFAD and control mice were used. All mice were fasted for at least 18 h prior to the imaging study. All mice were injected [$^{18}$F]nifene (PETNET intraperitoneally in normal saline (7.4 ± 0.7 MBq in 0.05–0.1 mL sterile saline) under 2% isoflurane (St. Joseph). They were placed in the supine position in a mouse holder and anesthetized with 2% isoflurane for whole-body PET/CT imaging. Note that 30-min long dynamic PET scans were acquired after [$^{18}$F]nifene injections, followed by a 7.5-min-long CT scan after the PET scan for attenuation correction and anatomical delineation of PET images. Nicotine (1 mg/kg, nicotine bitartrate salt in sterile saline, 0.1 mL, intraperitoneal [IP]) was administered to the mice while in the scanner bed and a second 30-min dynamic PET scan post-nicotine injection was acquired. Mice were then

awaken after [$^{18}$F]nifene injections and free to move in their cages for 2 h. The Inveon multimodality scanner was used for all combined PET/CT experiments.

## 2.8 | 5xFAD Mice [$^{18}$F]Nifene ex vivo autoradiography

After [$^{18}$F]nifene in vivo PET/CT experiments in control and 5xFAD mice, select mice were killed and the brain was excised. The brains containing [$^{18}$F]nifene were rapidly frozen at −80°C for approximately 10 min, followed by 10 min in the Leica cryotome at −20°C. Sagittal brain sections (10–40 $\mu$m thick) containing thalamus, subiculum, cortex, striatum, hippocampus, and cerebellum were cut using the Leica cryotome. The sections were rapidly air dried and subsequently apposed to phosphor films overnight. Films were read using the Cyclone Phosphor Imaging System. Regions-of-interest were drawn and analyzed on brain regions rich in $\alpha4\beta2^*$ nicotinic receptors using OptiQuant software and binding of [$^{18}$F]nifene measured in DLU/mm$^2$.

In order to assess A$\beta$ plaque load in the 5xFAD mice sagittal brain slices after [$^{18}$F]nifene PET experiments, in vitro studies using [$^{125}$I]IBETA were carried out on adjacent slices of the ex vivo brain. Ex vivo mice brain slices (10–40 $\mu$m thick) after 24 h fluorine-18 decay treated with [$^{125}$I]IBETA in 40% ethanol PBS buffer at pH 7.4 (60 mL; 1.5 kBq/mL) were incubated at 25°C for 1.25 h. Nonspecific binding was measured in the presence of 10 $\mu$M flotaza. The slices were then washed with cold PBS buffer (5 min), 90% ethanolic PBS buffer twice (5 min each), PBS buffer (5 min), and cold water (2 min). The brain sections were air dried, exposed for 1 week on a phosphor film, and then read on the Cyclone Storage Phosphor System. The amount of bound [$^{125}$I]IBETA in the autoradiograms was evaluated in various brain regions (as DLU/mm$^2$) using the OptiQuant acquisition and analysis program (Packard Instruments Co.). Select sections after fluorine-18 decay were also anti-A$\beta$ immunostained. Binding of [$^{18}$F]nifene was compared with [$^{125}$I]IBETA and anti-A$\beta$ immunostained adjacent 5xFAD brain slices of the same mouse.

## 2.9 | [$^{18}$F]FEPPA autoradiography in 5xFAD mice

In vitro autoradiography was carried out using [$^{18}$F]FEPPA, which is known to bind to TSPO as a biomarker for microglia. Brain slices (10 $\mu$m thick) from 5xFAD mice and control mice were used for the study. Brain slices were preincubated in 0.1 M Tris buffer at pH 7.4 for 15 min at room temperature. The slices were then treated with [$^{18}$F]FEPPA (Tris buffer 60 mL, 148 kBq/mL) and incubated for 1 h at 25°C. Nonspecific binding was measured in the presence of PK-11195 at concentration of 10 $\mu$M. The slices were then washed with cold Tris buffer twice (5 min each), followed by cold water (2 min). The brain sections were air dried, exposed overnight on a phosphor film, and then read on the Cyclone Storage Phosphor System. The amount of bound [$^{18}$F]FEPPA in the autoradiograms was evaluated in various brain regions (as DLU/mm$^2$) using the OptiQuant acquisition and analysis program (Packard Instruments Co.).

## 2.10 | Immunohistochemistry

Immunohistochemical (IHC) staining of all brain sections was carried out by University of California-Irvine, Pathology services using Ventana Benchmark Ultra protocols. To determine the localization of A$\beta$ accumulation in the subject brains, neighboring mouse brain slices (10 $\mu$m thick) from in vitro and ex vivo experiments were immunostained with anti-A$\beta$ Biolegend 803015 (Biolegend, CA, USA), which is reactive to amino acid residue 1–16 of A$\beta$. Immunostained sections were scanned using the Ventana Roche instrumentation, and the images were analyzed using QuPath software (Bankhead et al., 2017; Dunn et al., 2016; Mukherjee et al., 2022). Using QuPath, A$\beta$ plaque annotations were drawn on IHC images. Qupath was then used to train a machine learning classifier for A$\beta$ plaque for the entire slice. Measurements of the area of A$\beta$ plaque per $\mu$m$^2$ were obtained for various brain regions within a given slice. These measurements corresponded to the presence of A$\beta$ plaque load. Similarly, regions of interest drawn on autoradiographs of [$^{125}$I]IBETA using Optiquant of image intensity in DLU/mm$^2$ of brain regions were obtained and correlated with A$\beta$ plaque load obtained from IHC.

## 2.11 | Image analysis

All in vivo images were analyzed using the Inveon Research Workplace (IRW) software (Siemens Medical Solutions, Knoxville, TN, USA) and the PMOD software (PMOD Technologies, Zurich, Switzerland). Whole-body PET/CT images were analyzed using the IRW software for [$^{18}$F]nifene uptake and any other CT anomalies in the whole-body images. For brain quantitative analysis, brain images were analyzed using both IRW and PMOD. Using PMOD, PET images were coregistered to a mouse brain MRI template (Campoy et al., 2021; Coleman et al., 2017; Mondal et al., 2021; Ma et al., 2008). The magnitude of [$^{18}$F]nifene was expressed as standard uptake value (SUV), which was computed as the average [$^{18}$F]nifene

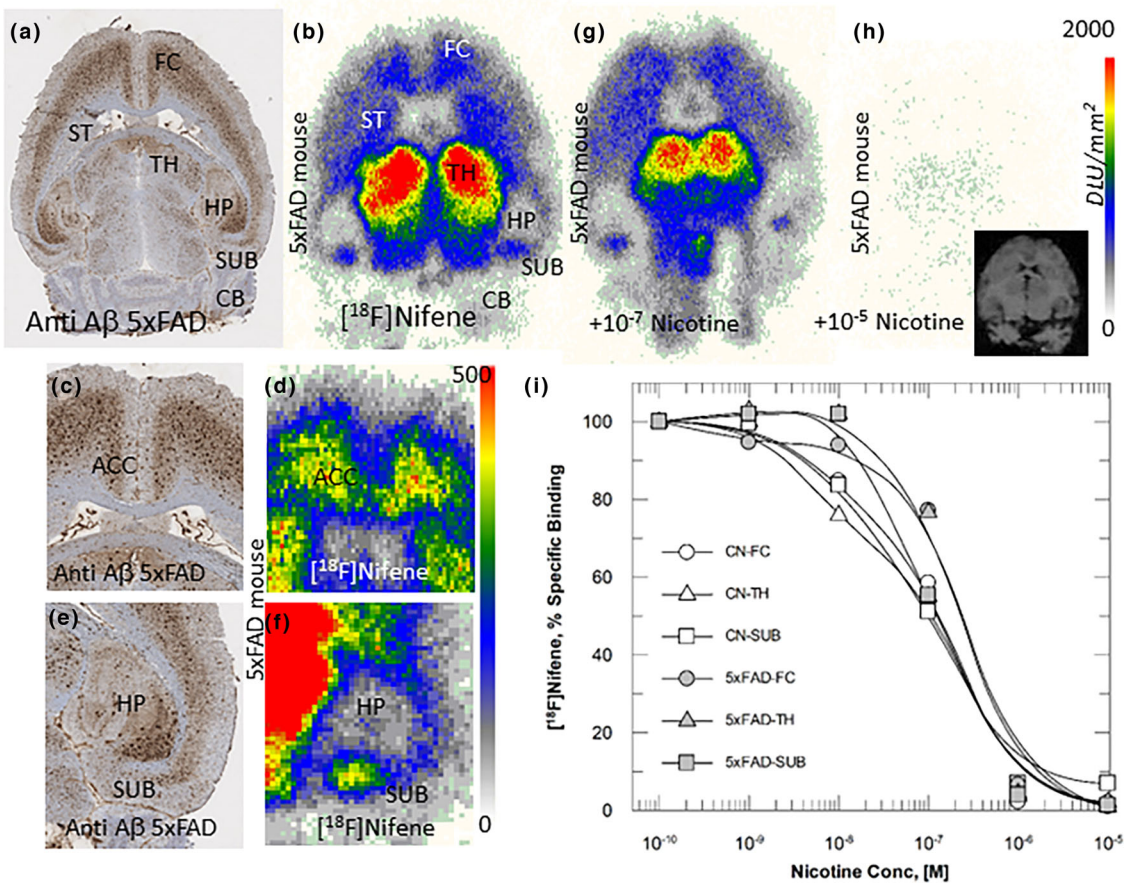


**FIGURE 2** In vitro [$^{18}$F]nifene in 5xFAD AD mice brain: (A) Anti-A$\beta$ immunostain of 10 $\mu$m brain slice of 5xFAD mouse confirming the presence of A$\beta$ plaques. (B) Total [$^{18}$F]nifene binding in brain slices of 5xFAD mouse showing high levels in thalamus (TH) and other extrathalmic regions with little binding in the cerebellum (CB). (C and D) Close-up view of FC immunostain and [$^{18}$F]nifene in 5xFAD mouse. (E and F) Close-up view of HP-SUB immunostain and [$^{18}$F]nifene in 5xFAD mouse. (G) [$^{18}$F]Nifene binding in brain slice of 5xFAD mouse in the presence of 0.1 $\mu$M nicotine. (H) [$^{18}$F]Nifene binding in brain slice of 5xFAD mouse in the presence of 10 $\mu$M nicotine where most of the [$^{18}$F]nifene is displaced (>95%); inset shows scan of brain slice. (I) Nicotine concentration effects on the specific binding of [$^{18}$F]nifene in 5xFAD and control mice brain slices in TH, FC and SUB. ACC, anterior cingulate cortex; FC, frontal cortex; HP, hippocampus; HP-SUB, hippocampus-subiculum ; ST, striatum; SUB, subiculum; TH, thalamus.

activity in each volume of interest (in kBq/mL) divided by the injected dose (in MBq) times the body weight of each animal (in kg). Using cerebellum SUV as the reference region, SUVR was calculated to compare different groups of mice. The SUV and SUVR values were then statistically analyzed using students *t*-test, and 5xFAD mice were compared with control mice.

## 3 | RESULTS

### 3.1 | In vitro [$^{18}$F]Nifene studies

Brain slices from 5xFAD mice exhibited significant amounts of A$\beta$ plaques as seen in the IHC stained section in Figure 2A. Distribution of A$\beta$ plaques was consistent with reported findings in this mouse model, with hippocampus and cortical areas showing high levels while the thalamus exhibited significant levels of plaques (Frost et al., 2020; Yin et al., 2022). Adjacent brain slices show [$^{18}$F]nifene binding in the expected regions of thalamus and frontal cortex including anterior cingulate regions, subiculum, and striatum with very little binding in the cerebellum (Figure 2B). Ratios of [$^{18}$F]nifene binding in brain regions versus cerebellum (CB) in 5xFAD mice were for thalamus (TH) = 17, hippocampus-subiculum (HP-SUB) = 7, frontal cortex (FC) = 5.5, and striatum (ST) = 4.7. This was similar to control mouse brain slices [$^{18}$F]nifene binding in all brain regions as previously reported (Campoy et al., 2021). Close-up views of frontal cortex with anterior cingulate region (Figure 2C,D) and hippocampus with subiculum regions (Figure 2E,F) show the presence of significant amounts of A$\beta$ plaques. These regions exhibited high levels of [$^{18}$F]nifene binding, except hippocampus which is known to contain fewer $\alpha 4\beta 2^*$ receptors except in the dentate gyrus.

**TABLE 1** Competition with [$^{18}$F]Nifene binding at nicotinic $\alpha4\beta2^*$ receptors

| Drug | Control mice brain slice[a] | | 5xFAD mice brain slice[a] | | Rat brain | |
|---|---|---|---|---|---|---|
| | Frontal cortex (nM) | Thalamus (nM) | Frontal cortex (nM) | Thalamus (nM) | Thalamus[a] (nM) | Homogenate[b] (nM) |
| Nicotine | 18 ± 3 | 16 ± 4 | 73 ± 10 | 31 ± 5 | 23.8 | 4.60 |
| Acetylcholine | 55 ± 7 | 34 ± 7 | 38 ± 6 | 83 ± 12 | – | 51.6 |

[a]Binding assay done autoradiographically with [$^{18}$F]nifene in brain slices.
[b]Binding assay with [$^{3}$H]cytisine in rat brain homogenates using reported methods (Easwaramoorthy et al., 2007).

In vitro binding of [$^{18}$F]nifene in both the 5xFAD and control mice was displaced by nicotine in a dose-dependent manner. [$^{18}$F]Nifene binding was reduced in the presence of 100 nM nicotine (Figure 2G) and >95% with 10 $\mu$M nicotine (Figure 2H) in the 5xFAD mice. Displacement curves of [$^{18}$F]nifene induced by nicotine in 5xFAD and control mice brain regions show >95% displacement at 10 $\mu$M nicotine in all brain regions. Affinities of nicotine for 5xFAD brain regions were somewhat weaker compared to control mice (Table 1). For frontal cortex of C57BL/6 mice, nicotine had an $IC_{50}$ = 18 nM ± 3 and for 5xFAD mice the $IC_{50}$ = 73 ± 10 nM ($p < .05$). In the case for thalamus nicotine affinities were 16 ± 4 nM for C57BL/6 and 31 ± 5 nM for 5xFAD mice ($p < .05$). Affinity of nicotine for [$^{18}$F]nifene displacement in the thalamus of C57BL/6 mice brain slices was approximately similar to our previously reported results in normal rat brain slices (Easwaramoorthy et al., 2007).

## 3.2 | Acetylcholine effects

Acetylcholine was used to study the displacement of [$^{18}$F]nifene in control mice and 5xFAD mice brain slices in vitro. Because ACh is rapidly hydrolyzed by AChE present in the brain slices, physostigmine, the AChEI drug, was used to prevent hydrolysis of ACh to choline by AChE, similar to our previous work in rat brain slices (Easwaramoorthy et al., 2007). Using [$^{18}$F]nifene, competition with ACh (1 nM to 10 $\mu$M) in the presence of 200 $\mu$M physostigmine was carried out in vitro in brain slices of control and 5xFAD mice. The amount of bound [$^{18}$F]nifene was assessed by autoradiography studies using 10-$\mu$m thick horizontal sections containing the thalamus, subiculum, cortex, striatum, hippocampus, and cerebellum. Figure 3A shows the binding of [$^{18}$F]nifene in a control brain slice. A significant reduction in the binding of [$^{18}$F]nifene was observed as seen in Figure 3B with 1 $\mu$M ACh. Similarly, ACh was able to displace [$^{18}$F]nifene binding in all regions of the brain slice as seen in Figure 3D versus total binding in Figure 3C in the 5xFAD brain slice. Figure 3E shows [$^{18}$F]nifene binding in two brain regions, frontal cortex and thalamus being displaced by increasing amounts of ACh. Affinity of acetylcholine in frontal cortex of C57BL/6 mice was $IC_{50}$ = 55 ± 10 nM and for 5xFAD mice $IC_{50}$ = 38 ± 6 nM ($p < .05$). Acetylcholine affinities in thalamus were 34 ± 7 nM for C57BL/6 mice and 83 ± 12 nM for 5xFAD mice ($p < .05$).

## 3.3 | In vitro [$^{125}$I]IBETA studies

The A$\beta$ plaque imaging agent, [$^{125}$I]IBETA, in the 5xFAD mice showed extensive binding in several brain regions (Figure 4A). TH, lateral septal nuclei (LSN), hippocampus (HP), SUB and FC regions showed high levels of [$^{125}$I]IBETA binding. Cerebellum (CER) had low levels of [$^{125}$I]IBETA nonspecific binding and would be suitable as a reference region for imaging studies. Ratio of brain regions versus cerebellum were very high (TH/CER > 15; LSN/CER > 13; HP/CER > 11; FC/CER > 7; SUB/CER > 6). Levels in the striatum (ST) were low (ST/CER > 2). Adjacent brain slices IHC stained revealed high A$\beta$ plaque levels in these brain regions (Figure 4B). A good correlation of binding of [$^{125}$I]IBETA with A$\beta$ plaque load was observed in the mice. Thalamus was an outlier, where greater amount of [$^{125}$I]IBETA was measured compared to the measured A$\beta$ plaque load (Figure 4A,B).

[$^{18}$F]Nifene binding in the 5xFAD mice brains correlated well with [$^{125}$I]IBETA in most of the brain regions suggesting overlapping locations of A$\beta$ plaques and $\alpha4\beta2^*$ receptors. Hippocampus and LSN have significant A$\beta$ plaque load (Figure 4B) and exhibit high levels of [$^{125}$I]IBETA binding (Figure 4A). However, [$^{18}$F]nifene has lower levels of binding in the hippocampus and LSN. On the other hand, significant [$^{18}$F]nifene binding in the nearby subiculum in mice is observed (Figure 2B,F). Therefore, hippocampus and LSN were outliers in the [$^{125}$I]IBETA -[$^{18}$F]nifene correlation plot (Figure 4C). But other regions (thalamus, frontal cortex, subiculum, and cerebellum) correlated well.

## 3.4 | Dynamic [$^{18}$F]Nifene PET/CT

Rapid uptake of [$^{18}$F]nifene was observed in brain regions of the C57BL/6 mouse brain, similar to our previous findings with the BALB/c mice (Campoy et al., 2021). Images at 60 min postinjection (Figure 5A) show high levels of [$^{18}$F]nifene in the thalamus, followed by extrathalamic regions including the frontal cortex. Harderian glands exhibited high nonspecific activity as previously reported in other mice species (Campoy et al., 2021). Time-activity curve in Figure 5B shows a progressive increase in [$^{18}$F]nifene uptake in the thalamus, frontal cortex and cerebellum, plateauing at

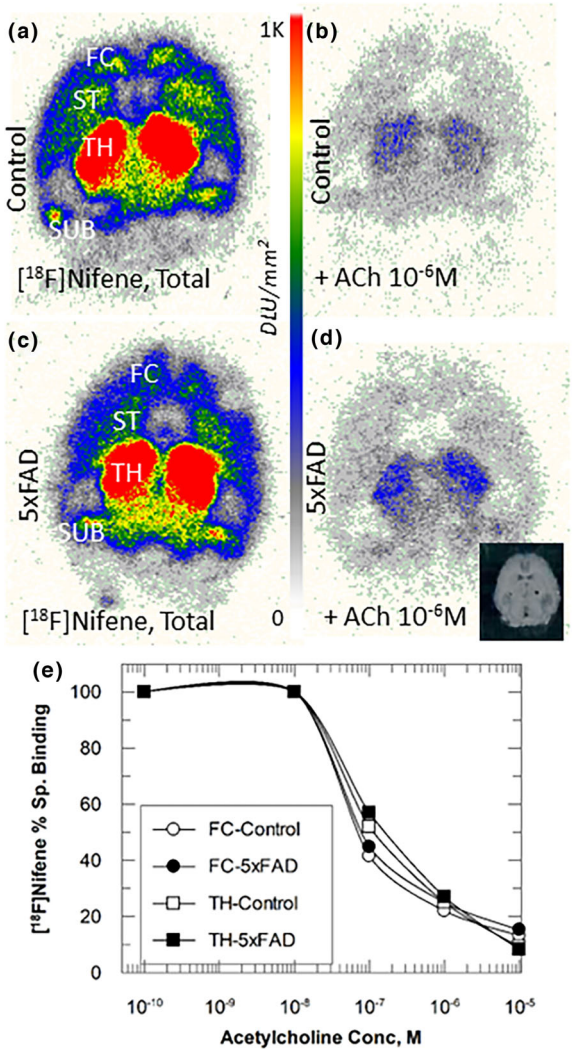


**FIGURE 3** Acetylcholine effects on [$^{18}$F]nifene: (A) Total binding of [$^{18}$F]nifene in control mouse brain 10 $\mu$m thick slice. (B) Acetylcholine (1 $\mu$M) displaces [$^{18}$F]nifene binding in control mouse brain slice. (C) [$^{18}$F]Nifene binding in brain 10 $\mu$m thick slice of 5xFAD mouse. (D) Acetylcholine (1 $\mu$M) displaces [$^{18}$F]nifene in brain slice of 5xFAD mouse (inset shows scan of brain slice). (E) Acetylcholine concentration effects in 5xFAD and control mice brain slices in vitro. CB, cerebellum; FC, frontal cortex; HP, hippocampus; ST, striatum; SUB, subiculum; TH, thalamus.

approximately 60 min postinjection and remaining steady with some clearance after 90 min. Thalamic regions exhibited the highest retention as it has a maximum amount of $\alpha4\beta2^*$ receptors, followed by the frontal cortex, with cerebellum as a reference region (Figure 5B). Ratio plot of thalamus and frontal cortex versus cerebellum shows a relatively flat profile after 30 min postinjection, with TH/CER = 2.3 and FC/CER = 1.7 at 117 min postinjection (Figure 5C).

Greater uptake of [$^{18}$F]nifene was observed in brain regions of the 5xFAD mouse brain. Images at 60 min postinjection (Figure 5D) show high levels of [$^{18}$F]nifene in the thalamus, followed by extrathalamic regions including the frontal cortex. Harderian glands exhibited similar high non-specific activity as seen in the control mice. Time-activity curve in Figure 5E shows a relatively more rapid increase in [$^{18}$F]nifene uptake in the thalamus, frontal cortex and cerebellum, peaking at approximately 40 min postinjection followed by some clearance after 60 min. Thalamic regions exhibited the highest retention as it has a maximum amount of $\alpha4\beta2^*$ receptors followed by the frontal cortex, with cerebellum as a reference region (Figure 5F). Ratio plot of thalamus was relatively flat, whereas the frontal cortex versus cerebellum exhibited a gradual increase in the ratio over time, with TH/CER = 2.5 and FC/CER = 2.10 at 117 min postinjection (Figure 5F). The FC/CER ratio was >20% in the 5xFAD mouse compared to control C57BL/6 mice.

## 3.5 | Static 5xFAD mice [$^{18}$F]Nifene PET/CT

Groups of control C57BL/6 mice ($n$ = 8) and 5xFAD mice ($n$ = 8) underwent [$^{18}$F]nifene PET/CT scans after IP injection and an uptake period of 30 min outside the scanner as described in Section 2.6. In the control mice, the distribution of [$^{18}$F]nifene was as expected with thalamus showing high

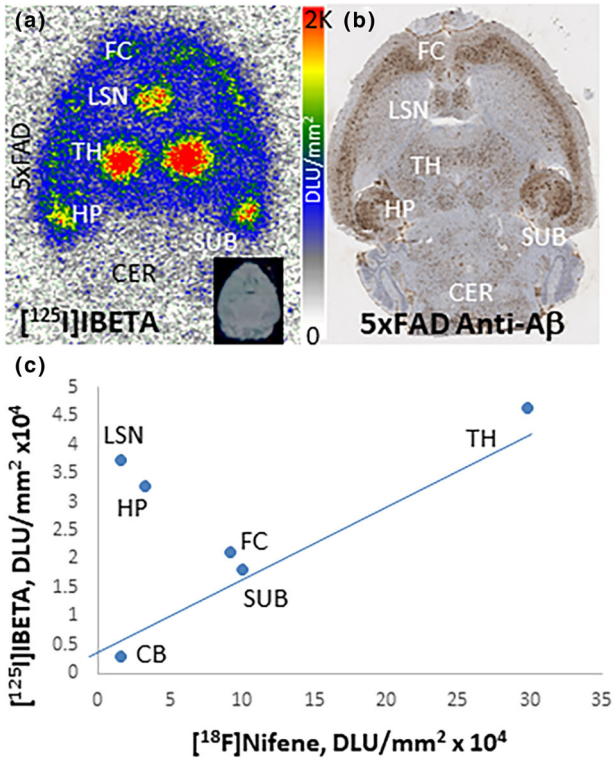


**FIGURE 4** In vitro [$^{125}$I]IBETA for A$\beta$ plaques in 5xFAD Mice: (A) [$^{125}$I]IBETA binding to A$\beta$ plaques in 10 $\mu$m brain slice of 5xFAD transgenic mice. (B) Adjacent slices immunostained with anti-A$\beta$ showing corresponding location of A$\beta$ plaques. (C) Correlation plot of [$^{125}$I]IBETA and [$^{18}$F]nifene (from Figure 2B) showing agreement in most regions except the hippocampus (HP) and lateral septal nuclei (LSN). CB, cerebellum; CER, cerebellum; FC, frontal cortex; HP, hippocampus; LSN, lateral septal nuclei; ST, striatum; SUB, subiculum; TH, thalamus.

levels, followed by frontal cortex and other extrathalamic regions (Figure 6A). Distribution in the 5xFAD mice was distinctly different. Frontal cortex exhibited higher levels of [$^{18}$F]nifene binding (Figure 6B). The amount of [$^{18}$F]nifene binding was similar or greater than the levels in the thalamus. Figure 6C shows SUVR (cerebellum as reference) comparisons in the thalamus and frontal cortex [$^{18}$F]nifene of the control group and 5xFAD group. Average [$^{18}$F]nifene SUVR in the FC of 5xFAD mice were significnatly higher than C57BL/6 mice (5xFAD mice FC = 3.04 and C57BL/6 mice FC = 1.92;$p$ = .001). Thalamus differences between 5xFAD mice (SUVR = 2.58) and C57BL/6 mice (SUVR = 2.38) were not significant. Frontal cortex 5xFAD mice SUVR was 159% higher than the control group. As shown in Figure 5E,F, frontal cortex exhibited greater retention in the 5xFAD mice compared to the control animals resulting in the higher frontal cortex [$^{18}$F]nifene in the 5xFAD transgenic mice.

## 3.6 | [$^{18}$F]Nifene PET-MR correlation

For anatomical localization of [$^{18}$F]nifene in the 5xFAD, the PET images of the brain of the control mice (Figure 7A) and the 5xFAD mouse (Figure 7B) were coregistered with the mouse brain template using PMOD. The high uptake in the bilateral regions outside of the brain corresponded to the regions outside the brain in the eyes and harderian glands. Uptake of other PET radiotracers have also been previously observed in these regions. Within the brain, in the control mice, high-binding region of [$^{18}$F]nifene corresponded to thalamus in the MRI, followed by lower levels of binding in the frontal cortex. Cerebellum had the least levels of binding similar to our previous findings with other mice species (Campoy et al., 2021; Zhang et al., 2022). The regional brain distribution of [$^{18}$F]nifene in the 5xFAD mice was different from the control brain. The major difference was the high uptake in the frontal cortical regions, whereas the thalamus was similar to the control mice as shown in Figure 7A,B [$^{18}$F]nifene PET-MRI coregistered images. In Figure 7C–E, horizontal brain slices of [$^{18}$F]nifene PET and MRI are shown at three different sagittal planes (superior to inferior). The high levels of [$^{18}$F]nifene localization in the 5xFAD mice appeared to be in the medial prefrontal cortex (mPFC) and anterior cingulate cortex (ACC) regions based on the coregistered MRI images in Figure 7C–E. This higher [$^{18}$F]nifene region aligns with reported anatomical location of mPFC (Kamigaki, 2019; Premachandran et al., 2020) and ACC (van Heukelum et al., 2020) in the mouse brain. Other extrathalamic brain regions such as hippocampus, subiculum, colliculi, and others were observed, but not quantitatively analyzed in this work. This will require additional in vivo–ex vivo [$^{18}$F]nifene imaging paradigm, as reported before in rat behavior studies (Bieszczad et al., 2012).

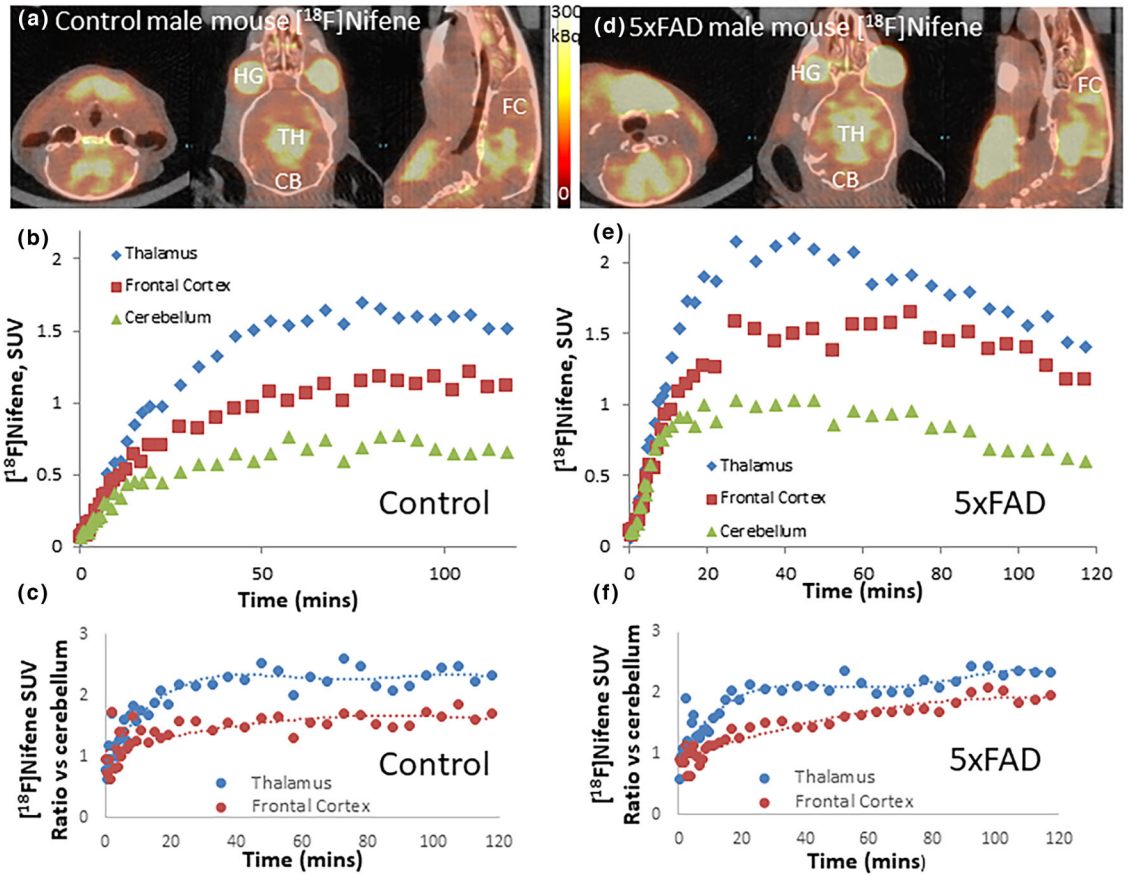


**FIGURE 5** In vivo [$^{18}$F]nifene in 5xFAD AD mice brain: (A) PET/CT of intraperitoneal (IP) [$^{18}$F]nifene (11 MBq in 50 $\mu$L saline) administered in control mouse (C57BL/6, male 42 g). Coronal, transaxial, and sagittal images of control mouse head at 60 min after injection showing [$^{18}$F]nifene in the brain. (B) Time-activity curve of thalamus, frontal cortex, and cerebellum in control mouse brain. (C) Ratio of thalamus and frontal cortex to cerebellum of time-activity curve in control mouse. (D) PET/CT of [$^{18}$F]nifene (6.25 MBq in 50 $\mu$L saline, IP) administered in AD mouse (5xFAD, male 30 g). Coronal, transaxial, and sagittal images of 5xFAD female mouse head at 60 min after injection showing [$^{18}$F]nifene in the brain. (E) Time-activity curve of thalamus, frontal cortex, and cerebellum in 5xFAD female mouse brain. (F) Ratio of thalamus and frontal cortex to cerebellum of time-activity curve in 5xFAD female mouse. CB, cerebellum; FC, frontal cortex; HG, harderian gland; SUV, standard uptake value; TH, thalamus.

## 3.7 | Nicotine challenge 5xFAD AD Mice [$^{18}$F]Nifene studies

Nicotine administration was carried out in the [$^{18}$F]nifene PET/CT studies of the control mice to ascertain in vivo displacement of [$^{18}$F]nifene. Figure 8A shows orthogonal brain slices of [$^{18}$F]nifene in the C57BL/6 mouse prior to injection of nicotine. Expected [$^{18}$F]nifene binding was seen in the thalamus and extrathalamic regions including the frontal cortex. Subsequent to nicotine administration (IP, 1 mg/kg), [$^{18}$F]nifene binding was displaced from all brain regions (Figure 8B). Time-activity curves in Figure 8C show increasing uptake of [$^{18}$F]nifene in the thalamus and frontal cortex, while cerebellum started to clear after an initial uptake period prior to injection of nicotine. Nicotine induced a rapid displacement of [$^{18}$F]nifene from both thalamus and frontal cortex of C57BL/6 mice, with off-rates (Figure 8D) greater for thalamus (koff = 0.027 min$^{-1}$; dissociation half life ($t_{1/2}$ = 0.693/koff), $t_{1/2}$ = 26 min) and frontal cortex (koff = 0.009 min$^{-1}$; $t_{1/2}$ = 77 min). Cerebellum had a koff = 0.007 min$^{-1}$ ($t_{1/2}$ = 99 min), reflective predominantly of the nonspecific clearance (k2) of [$^{18}$F]nifene. The displaceability of [$^{18}$F]nifene from all brain regions of normal mice is consistent with our recent findings (Zhang et al., 2022). The measured nicotine-induced thalamus off-rate of [$^{18}$F]nifene was similar to that previously reported for the rat thalamus computed using specific binding (koff = 0.06 min$^{-1}$, $t_{1/2}$ = 12 min; Kant et al., 2011).

Nicotine administration was carried out in the [$^{18}$F]nifene PET/CT studies of the 5xFAD mice to ascertain in vivo displacement of [$^{18}$F]nifene. Figure 9A shows orthogonal brain slices of [$^{18}$F]nifene in the 5xFAD mouse prior to injection of nicotine. Expected [$^{18}$F]nifene binding was seen in the thalamus and extrathalamic regions including the greater frontal cortex binding compared to control mice. Subsequent to nicotine administration (IP, 1 mg/kg), [$^{18}$F]nifene binding was displaced from brain regions except the frontal cortex (Figure 9B). Time-activity curves in Figure 9C show increasing uptake of [$^{18}$F]nifene in the thalamus and frontal cortex, while cerebellum started to clear after an initial uptake period prior to injection of nicotine. Nicotine induced a rapid displacement of [$^{18}$F]nifene from the thalamus, with off-rates (Figure 9D) for thalamus (koff = 0.019 min$^{-1}$; $t_{1/2}$

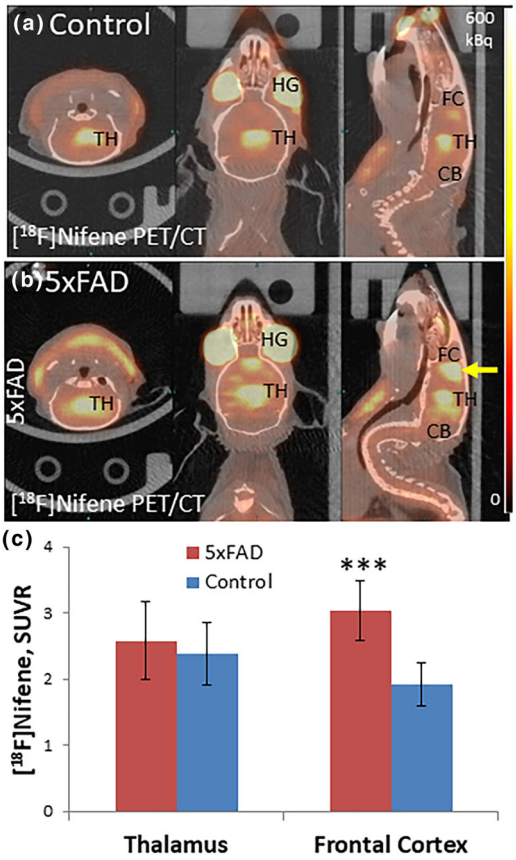


**FIGURE 6** 5xFAD mice [$^{18}$F]nifene PET/CT: (A) [$^{18}$F]Nifene in control group mice (male, 36 g, 2.1 MBq, intraperitoneal [IP]) showing binding in TH, FC, and low binding in CB with [$^{18}$F]nifene greater in TH compared to FC. (B) [$^{18}$F]Nifene in 5xFAD group mice (male, 20 g, 2.85 MBq, IP) showing binding in TH, FC, and low binding in CB with [$^{18}$F]nifene greater in TH lower or similar compared to FC. (C) Bar graph comparing averages of control ($n = 6$) and 5xFAD ($n = 6$) in TH and FC SUVR (CB as reference). Differences in [$^{18}$F]nifene TH binding between the two groups were not significant, but the [$^{18}$F]nifene FC in 5xFAD was higher and very significant ($p = .001$) when compared to controls. CB, cerebellum; FC, frontal cortex; HG, harderian gland; TH, thalamus.

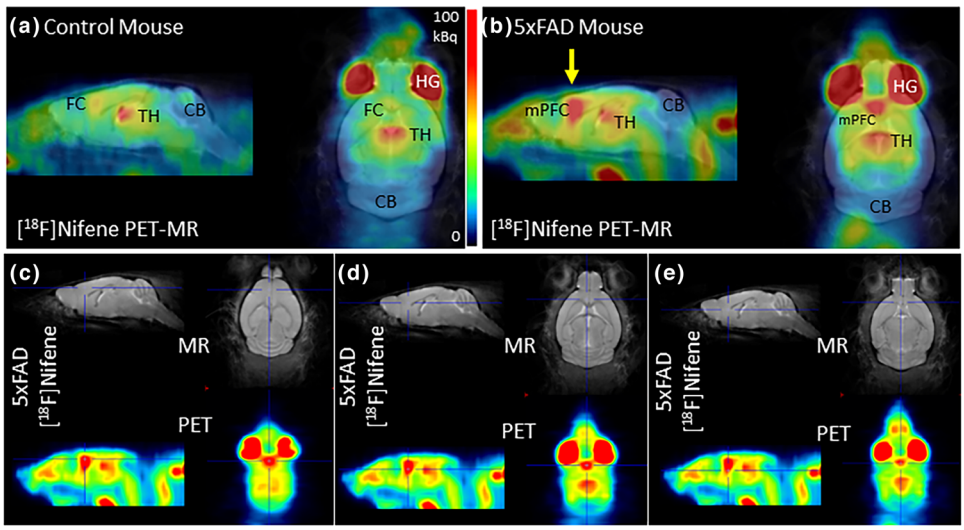


**FIGURE 7** PET-MR of [$^{18}$F]nifene 5xFAD mice: (A) Coregistered [$^{18}$F]nifene PET-MR control mouse C57BL/6, sagittal and coronal brain sections. (B) Coregistered [$^{18}$F]nifene PET-MR mouse 5xFAD, sagittal and coronal brain sections. (C–E) Three superior to inferior planes of coregistered [$^{18}$F]nifene PET-MR 5xFAD mouse with cross hairs placed on the medial prefrontal cortex/anterior cingulate in sagittal and transaxial brain sections. AC, anterior cingulate; CB, cerebellum; HG, harderian gland; mPFC, medial prefrontal cortex; TH, thalamus.

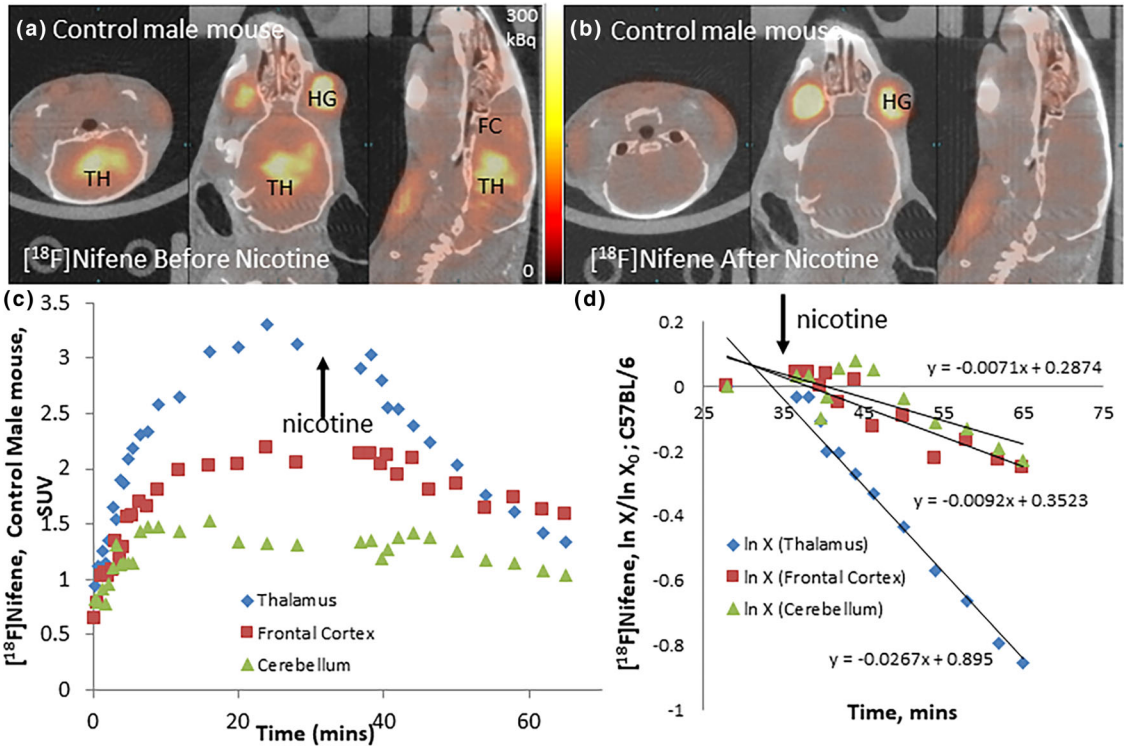


**FIGURE 8** Nicotine effects on [$^{18}$F]nifene in C57BL/6 mice: (A) PET/CT of [$^{18}$F]nifene (7.4 MBq, intraperitoneal [IP]) in control C57BL/6 mouse male (46 g) showing coronal, transaxial, and sagittal images at 30 min before nicotine administration. (B) Coronal, transaxial, and sagittal images at 30 min after nicotine (1 mg/kg, IP). (C) Time-activity curve of thalamus, frontal cortex, and cerebellum showing nicotine intervention (arrow). (D) Dissociation rate (ln $X/X_0$) plot for thalamus ($k_{off}$ = 0.027 min$^{-1}$), frontal cortex ($k_{off}$ = 0.009 min$^{-1}$), and cerebellum ($k_{off}$ = 0.007 min$^{-1}$).

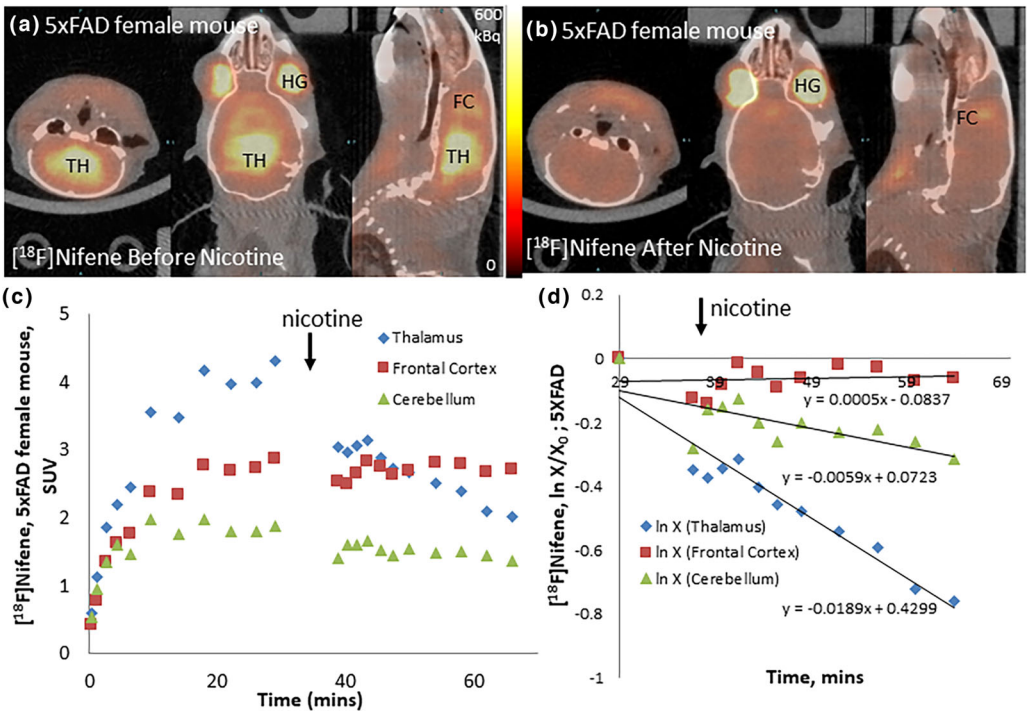


**FIGURE 9** Nicotine effects on [$^{18}$F]nifene in 5xFAD mice: (A) PET/CT of [$^{18}$F]nifene (5 MBq, intraperitoneal [IP]) in 5xFAD mouse female (20 g) showing coronal, transaxial, and sagittal images at 30 min before nicotine administration. (B) Coronal, transaxial, and sagittal images 30 min after nicotine (1 mg/kg, IP). (C) Time-activity curve of thalamus, frontal cortex, and cerebellum showing nicotine intervention (arrow). (D) Dissociation rate (ln $X/X_0$) plot for thalamus ($k_{off}$ = 0.035 min$^{-1}$) and cerebellum ($k_{off}$ = 0.006 min$^{-1}$). Frontal cortex shows no dissociation in the 5xFAD mouse but continues to increase at a rate of 0.0005 min$^{-1}$.

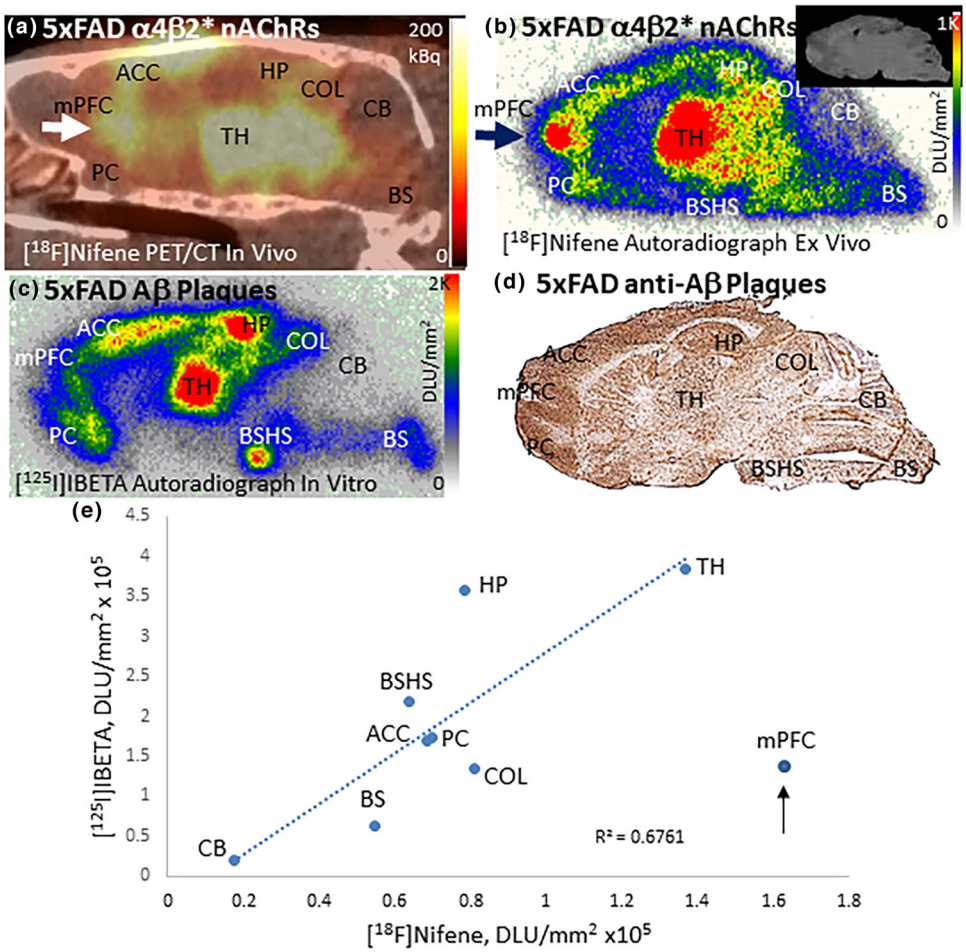


**FIGURE 10** Ex vivo [$^{18}$F]Nifene and [$^{125}$I]IBETA in 5xFAD mice: (A) Sagittal in vivo PET/CT [$^{18}$F]nifene image in 5xFAD mouse brain at approximately 70 min post-injection (male 26 g; 7.4 MBq intraperitoneal [IP]). (B) Ex vivo [$^{18}$F]nifene autoradiograph (10 $\mu$m thick slice) of same mouse after PET/CT experiment. (C) In vitro autoradiograph of adjacent brain slice of same mouse (after fluorine-18 decay) labeled with [$^{125}$I]IBETA for A$\beta$ amyloid plaques. (D) In vitro immunostain of adjacent brain slice (after fluorine-18 decay) labeled with anti-A$\beta$ for A$\beta$ amyloid plaques. (E) Correlation of [$^{125}$I]IBETA labeled A$\beta$ plaques with [$^{18}$F]nifene binding ($r^2 = 0.68$). The outlier, mPFC was not used in the correlation. AC, anterior cingulate; BS, brain stem; BSHS, brain stem hot spot; CB, cerebellum; COL, colliculi; HP, hippocampus; mPFC, frontal cortex; PC, piriform cortex; TH, thalamus.

= 37 min). Frontal cortex [$^{18}$F]nifene was not displaceable by nicotine, although cerebellum had a koff = 0.006 min$^{-1}$ ($t_{1/2}$ = 116 min) in the 5xFAD mice, suggestive of nonspecific clearance of [$^{18}$F]nifene similar to the C57BL/6 mice. In addition, the measured nicotine-induced thalamus off-rate of [$^{18}$F]nifene for the 5xFAD mice was slower than the C57BL/6 mice. The non-displaceability of frontal cortex [$^{18}$F]nifene was also evident from the retention of [$^{18}$F]nifene in the frontal cortex in the time-activity curve (Figure 9C), while thalamus activity continued to decrease.

## 3.8 | Ex vivo [$^{18}$F]Nifene—[$^{125}$I]IBETA comparison in 5xFAD mice

After the [$^{18}$F]nifene PET/CT scan of the 5xFAD mouse (Figure 10A, sagittal brain slice showing [$^{18}$F]nifene bound to the thalamus, frontal cortex, and other brain regions), the 5xFAD mouse was killed, 80 min postinjection of [$^{18}$F]nifene and the brain was excised immediately. The brain was rapidly frozen and sagittal brain sections were obtained. Figure 10B shows a sagittal brain section showing [$^{18}$F]nifene bound to the thalamus, frontal cortex, and other brain regions. Binding of [$^{18}$F]nifene in the ex vivo brain slice (Figure 10B) from the same mouse followed the general pattern on in vivo binding (Figure 10A). Thalamus was clearly the high-binding region. The "hot spot" in the frontal cortex was evident in both the in vivo PET scan and the ex vivo autoradiograph. Smaller regions such the subiculum was seen in the ex vivo image but were not clearly visualized in the in vivo scans. As expected, cerebellum had the least amount of activity both in vivo and ex vivo.

After the radioactive decay of [$^{18}$F]nifene from the stored (−80°C) sagittal brain slices, select slices were evaluated for the presence of A$\beta$ plaques by anti-A$\beta$ amyloid IHC (Figure 10D) and by [$^{125}$I]IBETA autoradiography (Figure 10C). Figure 10C shows in vitro binding of [$^{125}$I]IBETA in an

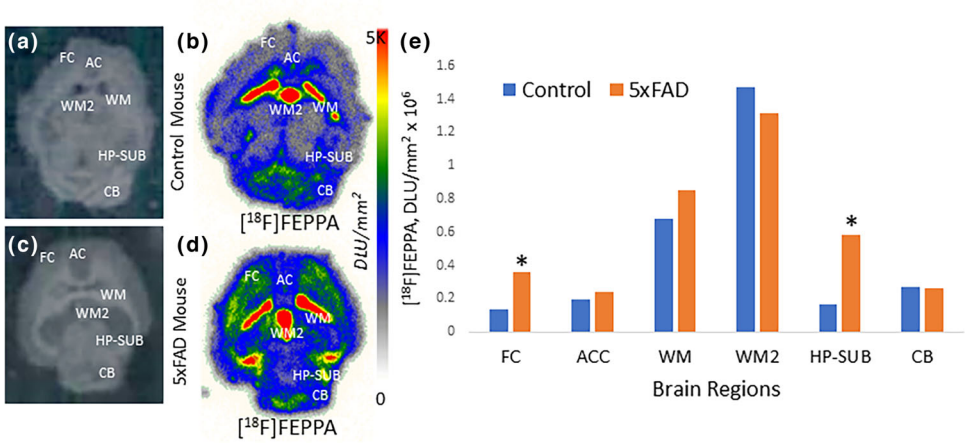


**FIGURE 11** In vitro [$^{18}$F]FEPPA in 5xFAD mice: (A) Control brain slice 10 $\mu$m scan showing various regions. (B) [$^{18}$F]FEPPA binding in the 10 $\mu$m brain slice of control mice. (C) 5xFAD brain slice 10 $\mu$m scan showing various regions. (D) [$^{18}$F]FEPPA binding in 10 $\mu$m brain slice of 5xFAD transgenic mice. (E) Comparison of [$^{18}$F]FEPPA binding between control and 5xFAD mice. Significantly higher binding of [$^{18}$F]FEPPA was seen in FC and HP-SUB. AC, anterior cingulate; CB, cerebellum; FC, frontal cortex; HP, hippocampus; SUB, subiculum; WM and WM2, white matter.

adjacent brain slice of the same 5xFAD mouse with high levels in the thalamus, hippocampus, cortical regions, brain stem, and colliculi. Cerebellum levels were close to background levels. [$^{18}$F]Nifene and [$^{125}$I]IBETA levels in the different regions were correlated ($r^2 = 0.68$) as shown in Figure 10E. Because of the high levels of [$^{18}$F]nifene in the mPFC, it is seen as an outlier in Figure 10E.

### 3.9 | In vitro [$^{18}$F]FEPPA studies

The TSPO imaging agent, [$^{18}$F]FEPPA, in the mice showed extensive binding in several brain regions (Figure 11B,D). Regions of the white matter (WM and WM2) in both the C57BL/6 and 5xFAD mice slices were high. This is consistent with the binding properties of [$^{18}$F]FEPPA in mice as well as other species (Vignal et al., 2018). Two brain regions where the 5xFAD mice showed significantly higher levels of [$^{18}$F]FEPPA binding compared to the C57BL/6 mice were FC and HP-SUB. The higher [$^{18}$F]FEPPA binding in these two regions is consistent with reports of other TSPO PET radiotracers in these regions (Mirzaei et al., 2016; Rejc et al., 2022). Ratio of brain regions versus CB for the C57BL/6 mice brains was FC/CB = 0.50, ACC/CB = 0.60, and HP-SUB/CB = 0.71, suggesting that CB had more nonspecific binding (Figure 11E).

In the case of 5xFAD mice brain slices, ratio of brain regions versus CB was FC/CB = 1.38, ACC/CB = 0.92, and HP-SUB/CB = 2.24, suggesting significantly increased TSPO levels and microglia in the 5xFAD mice (Figure 11E). Binding of [$^{18}$F]FEPPA in these regions overlapped with both [$^{18}$F]nifene and [$^{125}$I]IBETA binding in the 5xFAD mice brains.

## 4 | DISCUSSION

The 5xFAD mice expressing A$\beta$ plaques were found to be an excellent model to examine potential alterations in $\alpha4\beta2^*$ nAChRs. The presence of A$\beta$ plaques in these mice were confirmed in these mice using [$^{124/125}$I]IBETA and anti-A$\beta$ IHC (Nguyen et al., 2022) and [$^{18}$F]flotaza (Kaur et al., 2021) and were consistent with the findings of [$^{18}$F]florbetaben (Boulter et al., 2021). In vitro binding of [$^{125}$I]IBETA and [$^{124}$I]IBETA in transgenic 5xFAD mouse model for A$\beta$ plaques was high in the frontal cortex, anterior cingulate, thalamus, and hippocampus, which were regions of high A$\beta$ accumulation, with very little binding in the cerebellum (ratio of brain regions to cerebellum was >5). This in vitro binding of [$^{125}$I]IBETA and [$^{124}$I]IBETA was also observed in postmortem human AD brains gray matter containing A$\beta$ plaques compared to WM (Nguyen et al., 2022). Anti-A$\beta$ immunostaining strongly correlated with [$^{124}$/$^{125}$I]IBETA regional binding in both 5xFAD mouse and postmortem AD human brains. These observations suggested the similarity of the binding sites in the 5xFAD mice and human AD brain. Preliminary PET/CT studies of [$^{124}$I]IBETA in the 5xFAD mouse model showed greater localization of [$^{124}$I]IBETA in the brain regions with a high concentration of A$\beta$ plaques (Nguyen et al., 2022). Thus, the 5xFAD mice provided a good A$\beta$ plaque model to study effects on the $\alpha4\beta2^*$ nAChRs.

In vitro binding of [$^{18}$F]nifene in the 5xFAD mice brain sections was similar to the control mice (Campoy et al., 2021). Thalamus exhibited the highest levels, followed by anterior cingulate cortex, frontal cortex, subiculum, and striatum, and the least levels were in the cerebellum. These brain regions exhibited abundant A$\beta$ plaques except for striatum and cerebellum. [$^{18}$F]Nifene binding was low in the hippocampus of 5xFAD mice, a region known to contain high A$\beta$ plaque load. The low hippocampus binding in 5xFAD mice is similar to findings in the control mice hippocampus

(Campoy et al., 2021). Nicotine, due to its high affinity to $\alpha4\beta2^*$ receptors (Mukherjee et al., 2018), displaced [$^{18}$F]nifene in brain slices in vitro. A total of 10 $\mu$M nicotine was able to displace [$^{18}$F]nifene from all brain regions in the 5xFAD mice including thalamus, anterior cingulate cortex, and subiculum (Figure 2H). Displacement of [$^{18}$F]nifene in the 5xFAD mice regions may reflect the slightly weaker affinity of nicotine in the 5xFAD mice and the effect of A$\beta$ plaque and/or microglia related pathology.

Acetylcholine was able to displace [$^{18}$F]nifene from both control mice and 5xFAD brain slices. Since ACh is rapidly hydrolyzed by AChE present in the brain slices, treatment with physostigmine, a AChEI, was necessary, as previously reported in our rat brain studies (Easwaramoorthy et al., 2007). [$^{18}$F]Nifene was displaced by ACh from control mice and 5xFAD mice horizontal sections containing the thalamus, subiculum, cortex, striatum, hippocampus, and cerebellum (Figure 3A–D). All regions showing [$^{18}$F]nifene binding were decreased in the presence of Ach, as shown in Figure 3. Studies have been carried out to understand the association of A$\beta$ plaques and nicotinic receptors (Wu et al., 2004), altered acetylcholinesterase (AChE) glycosylation in AD pathology in Tg2576 mice (Fodero et al., 2002), AChE acting as a nucleating factor (Rees et al., 2003), and cortical cholinergic neurodegenerative changes occurring before the deposition of A$\beta$-containing neuritic plaques (German et al., 2003).

Regional in vivo brain uptake of [$^{18}$F]nifene in thalamic and extrathalamic regions in the 5xFAD mice was similar to the C57BL/6 mice (Figure 5A,D). Thalamus showed the highest levels, followed by frontal cortex and the least in the cerebellum as seen in the time-activity curves (Figure 5B,E). Ratio plots of the two regions versus cerebellum showed plateauing at approximately 2.2 for the thalamus and 1.6 for frontal cortex in the C57BL/6 mice, which is consistent with our previous observations (Campoy et al., 2021). Ratio of thalamus to cortex at the end of the scan was 1.3–1.5 in C57BL/6 mice. In the case of the 5xFAD mice, ratio plots of the two regions versus cerebellum showed plateauing in the thalamus at approximately 2.2, but frontal cortex continued to rise, suggesting nonreversible binding of [$^{18}$F]nifene. Ratio of thalamus to cortex at the end of the scan was 1.1 in the 5xFAD mice. This [$^{18}$F]nifene binding in the frontal cortex in the 5xFAD mice was a significant deviation from observations in the control C57BL/6 mice and our previously reported control BALB mice (Campoy et al., 2021).

For comparing [$^{18}$F]nifene binding in groups of C57BL/6 and 5xFAD mice, after the CT scan, a static PET scan between approximately 40–70 min post intraperitoneal administration of [$^{18}$F]nifene was acquired. Control C57BL/6 mice showed normal distribution in the thalamus and frontal cortex (Figure 6A,C) with average SUVR of 2.38 for thalamus and 1.92 for frontal cortex. In the case of 5xFAD, frontal cortex showed significantly higher SUVR (3.04) compared to the control C57BL/6 mice (Figure 6B,C). Further detailed analysis of [$^{18}$F]nifene bound to the C57BL/6 and 5xFAD mouse brain was carried out by using coregistration of [$^{18}$F]nifene PET with mouse brain MR template (Figure 7). Thalamic and extrathalamic regions were confirmed using the PET-MR coregistered images, including the extracranial localization in the vicinity of the harderian glands in both C57BL/6 and 5xFAD mice (Figure 7A,B). Evaluation across the different planes (Figure 7C,D) of the 5xFAD brain suggests very focused [$^{18}$F]nifene localization in the anterior cingulate cortex and medial prefrontal cortex, brain regions critical for executive control (Kamigaki, 2019; Premachandran et al., 2020; Van Heukelum et al., 2020).

In the PET study shown in Figure 8, nicotine was able to displace [$^{18}$F]nifene bound to the thalamus and frontal cortex in the C57BL/6 mice, which was consistent with our previous findings in mice, rats and monkeys (Hillmer et al., 2011; Kant et al., 2011; Zhang et al., 2022). In the case of the 5xFAD mice, thalamic [$^{18}$F]nifene binding was displaced, but the frontal cortex binding was nondisplaceable with the nicotine dose used (Figure 9). The dissociation half life (off-rate) of [$^{18}$F]nifene from the thalamus in the 5xFAD mice was slower compared to the C57BL/6 mice thalamus. The inability to displace [$^{18}$F]nifene from the frontal cortex in 5xFAD mice compared to the C57BL/6 mice was striking. This can be seen in Figure 9, where both thalamus and cerebellum continue to decrease, while frontal cortex has a gradual increase in binding.

In order to further understand the mPFC binding of [$^{18}$F]nifene, ex vivo studies were carried out on the 5xFAD mice after the PET/CT scan. Ex vivo autoradiography of the 5xFAD brain after the in vivo PET/CT scan confirmed the high [$^{18}$F]nifene binding in the AC/mPFC (Figure 10B), consistent with what was observed in the in vivo PET/CT (Figure 10A). Adjacent ex vivo brain slices after fluorine-18 decay were labeled with [$^{125}$I]IBETA and the presence of A$\beta$ plaques in the various regions was confirmed (Figure 10C). Correlation of [$^{125}$I]IBETA binding to A$\beta$ plaques with [$^{18}$F]nifene binding appeared strong except for hippocampus and anterior cingulate. Adjacent slices with anti-A$\beta$ immunostains correlated with [$^{125}$I]IBETA (Figure 10E–G). Thalamic A$\beta$ plaques are reportedly formed at later ages and have been reported to be structurally different from the frontal cortex A$\beta$ plaques, which are formed early in AD (Aggleton et al., 2016; Wengenack et al., 2011). Could this difference in the nature of A$\beta$ plaque between the thalamus and frontal cortex attribute to the difference in nicotine effects on [$^{18}$F]nifene in the two brain regions?

Since microglia play a very significant role in the 5xFAD mice (Forner et al., 2021), a preliminary in vitro autoradiographic study was carried out to evaluate in brain slices comparing the 5xFAD with C57BL/6 mice (Figure 11). Consistent with previous reports, [$^{18}$F]FEPPA showed increased binding in the frontal cortex and hippocampus-subiculum regions in the 5xFAD mice. Anterior cingulate or medial prefrontal cortex did not show any particularly high concentration compared to the frontal cortex. It is likely that the increased [$^{18}$F]nifene binding in the FC/AC/mPFC may be due to both the presence of A$\beta$ plaques and microglia.

But the irreversibility of [$^{18}$F]nifene binding in the FC/AC/mPFC remains unresolved. This unusual binding of [$^{18}$F]nifene is unlikely due to potential microbleeds (Cacciottolo et al., 2021; Koveri et al., 2015; Shih et al., 2018). Our results (data not shown) with sodium [$^{18}$F]fluoride to assess any blood brain barrier (BBB) disruption did not show any brain uptake. Brain metastasis with BBB disruption has been imaged using sodium [$^{18}$F]fluoride (Gori et al., 2015). Similarly, our results (data not shown) with [$^{18}$F]FDG and other reported findings of [$^{18}$F]FDG in the 5xFAD mice have not reported any unusual frontal cortex increases (Franke et al., 2020; Macdonald et al., 2014), thus potentially ruling out BBB disruption. Studies on rats with ischemia exhibited increased binding of [$^{18}$F]2-FA85380, another nAChR PET imaging agent in the cortical regions (Martín et al.,

2015). Overexpression of $\alpha4\beta2^*$ receptors was observed in microglia/macrophages and astrocytes. Although 5xFAD mice have not been shown to experience ischemia, the presence of abundant microglia in the 5xFAD mice is well known (Forner et al., 2021) including our findings of increased [$^{18}$F]FEPPA in the 5xFAD mice. Perhaps our findings suggest that the molecular nature of in vivo [$^{18}$F]nifene binding in the FC/AC/mPFC of 5xFAD mice is different compared to the C57BL/6 mice. Since PFC is innervated with nicotinic receptors (Koukouli et al., 2016), altered or dysfunctional nicotinic receptors in the mPFC are likely to adversely affect cholinergic functions in the 5xFAD mice resulting in impaired cognitive processes.

## 5 | CONCLUSION

The 5xFAD transgenic mice provided a useful model to study the effects of A$\beta$ plaques and microglia on $\alpha4\beta2^*$ nAChRs. A major finding is the high, non-displaceable binding of [$^{18}$F]nifene in the FC/mPFC/ACC. Does the increased [$^{18}$F]nifene binding in FC/mPFC/ACC in the 5xFAD mice suggest a compensatory mechanism against A$\beta$ pathology? The irreversibility and inability of nicotine to displace in vivo [$^{18}$F]nifene raise several possibilities: (1) An interaction of A$\beta$ oligomers, fibrils, or plaques with the $\alpha4\beta2^*$ receptor alters pharmacological properties of the receptor and affects the binding of [$^{18}$F]nifene and nicotine. (2) The ability of [$^{18}$F]nifene to bind and an inability of nicotine to displace receptor bound [$^{18}$F]nifene in the 5xFAD mice suggest additional interactions of [$^{18}$F]nifene at the receptor site or an alternate site, such as the microglia, rendering it irreversible. (3) If acetylcholine is similarly affected like [$^{18}$F]nifene, does it render the receptor hyperactive or desensitized and nonfunctional? (4) Does this have implications on AChEI, which are used to elevate acetylcholine levels in AD subjects?

### AUTHOR CONTRIBUTIONS

All authors had full access to all the data in the study and take responsibility for the integrity of the data and the accuracy of the data analysis. *Study concept and design*: Jogeshwar Mukherjee. *Acquisition of data*: Christopher Liang, Grace A. Nguyen, Tram B. Danh, and Jogeshwar Mukherjee. *Analysis and interpretation of data*: Christopher Liang, Anoopraj K. Sandhu, Lusine L. Melkonyan, Amina U. Syed, and Jogeshwar Mukherjee. *Drafting of the manuscript*: Jogeshwar Mukherjee and Christopher Liang. *Statistical analysis*: Christopher Liang and Jogeshwar Mukherjee. *Obtained funding*: Jogeshwar Mukherjee. *Study supervision*: Jogeshwar Mukherjee.

### ACKNOWLEDGMENTS

Research support for this study was provided by NIH AG RF1 AG029479 and the Undergraduate Research Opportunities Program at University of California, Irvine. We thank Jeffrey Kim, Pathology and Laboratory Medicine, University of California-Irvine for immunostaining of brain sections. We would also like to thank MODEL-AD UCI consortium (NIA AG054349) for support with the transgenic mice.

### CONFLICT OF INTEREST STATEMENT

The authors declare no conflict of interest.

### DATA AVAILABILITY STATEMENT

The data that support the findings of this study are available from the corresponding author upon reasonable request.

### REFERENCES

Aggleton, J. P., Pralus, A., Nelson, A. J. D., & Hornberger, M. (2016). Thalamic pathology and memory loss in early Alzheimer's disease: Moving the focus from the medial temporal lobe to Papez circuit. *Brain*, *139*, 1877–1890.

Bankhead, P., Loughrey, M. B., Fernandez, J. A., Dombrowski, Y., McArt, D. G., Dunne, P. D., McQuaid, S., Gray, R. T., Murray, L. J., Coleman, H. G., James, J. A., Salto-Tellez, M., & Hamilton, P. W. (2017). QuPath: Open source software for digital pathology image analysis. *Scientific Reports*, *7*, 16878.

Bieszczad, K. M., Kant, R., Constantinescu, C. C., Pandey, S. K., Kawai, H. D., Metherate, R., Weinberger, N. M., & Mukherjee, J. (2012). Nicotinic acetylcholine receptors in rat forebrain that bind ź$^8$F-nifene: Relating PET imaging, autoradiography, and behavior. *Synapse*, *66*, 418–434.

Boulter, C., Irwin, C., Frankle, T. N., Beindorff, N., & Boulter, Y. (2021). Quantitative brain positron emission tomography in female 5xFAD Alzheimer mice: Pathological features and sex-specific alterations. *Frontiers Medicine*, *8*, 745064. https://doi.org/10.3389/fmed.2021.745064

Braak, H., Thal, D. R., Ghebremedhin, E., & Del Tredici, K. (2011). Stages of the pathologic process in Alzheimer disease: Age categories from 1 to 100 years. *Journal of Neuropath & Experimental Neurology*, *70*(11), 960–969.

Cacciottolo, M., Morgan, T. E., & Finch, C. E. (2021). Age, sex, and cerebral microbleeds in EFAD Alzheimer's disease mice. *Neurobiology Aging*, *103*, 42–51.

Campoy, A.-D. T., Liang, C., Ladwa, R. M., Patel, K. K., Patel, I. H., & Mukherjee, J. (2021). [$^{18}$F]Nifene PET/CT imaging in mice: Improved methods and preliminary studies of $\alpha4\beta2^*$ nicotinic acetylcholinergic receptors in transgenic A53T mouse model of $\alpha$-synucleinopathy and post-mortem human Parkinson's disease. *Molecules (Basel, Switzerland)*, *26*, 7360.

Coleman, R. A., Liang, C., Patel, R., Ali, S., & Mukherjee, J. (2017). Brain and brown adipose tissue metabolism in transgenic Tg2576 mice models of Alzheimer disease assessed using 18F-FDG PET imaging. *Molecular Imaging*, *16*, 1536012117704557. https://doi.org/10.1177/1536012117704557

Colloby, S. J., Perry, E. K., Pakrasi, S., Pimlott, S. L., Wyper, D. J., McKeith, I. G., Williams, E. D., & O'Brien, J. T. (2010). Nicotinic 123I-5IA-85380 single photon emission computed tomography as a predictor of cognitive progression in Alzheimer's disease and dementia with Lewy bodies. *The American Journal of Geriatric psychiatry: Official Journal of the American Association for Geriatric Psychiatry*, *18*(1), 86–90. https://doi.org/10.1097/JGP.0b013e3181b972aa

Constantinescu, C. C., Garcia, A., Mirbolooki, M. R., Pan, M. L., & Mukherjee, J. (2013). Evaluation of [18F]Nifene biodistribution and dosimetry based on whole-body PET imaging of mice. *Nuclear Medicine and Biology*, *40*(2), 289–294. https://doi.org/10.1016/j.nucmedbio.2012.11.004

Constantinescu, C. C., & Mukherjee, J. (2009). Performance evaluation of an Inveon PET preclinical scanner. *Physics in Medicine and Biology*, *54*(9), 2885–2899. https://doi.org/10.1088/0031-9155/54/9/020

Coyle, J. T., Price, D. L., & DeLong, M. R. (1983). Alzheimer's disease: A disorder of cortical cholinergic innervation. *Science (New York, N.Y.)*, *219*(4589), 1184–1190. https://doi.org/10.1126/science.6338589

Desmarais, J. E., & Gauthier, S. (2010). Alzheimer disease: Clinical use of cholinergic drugs in Alzheimer disease. *Nature Reviews Neurology*, *6*(8), 418–420. https://doi.org/10.1038/nrneurol.2010.105

Dunn, W. D., Gearing, M. Jr, Park, Y., Zhang, L., Hanfelt, J., Glass, J. D., & Gutman, D. A. (2016). Applicability of digital analysis and imaging technology in neuropathology assessment. *Neuropathology: Official Journal of the Japanese Society of Neuropathology*, *36*(3), 270–282. https://doi.org/10.1111/neup.12273

Easwaramoorthy, B., Pichika, R., Collins, D., Potkin, S. G., Leslie, F. M., & Mukherjee, J. (2007). Effect of acetylcholinesterase inhibitors on nicotinic $\alpha4\beta2$ receptor PET radiotracer, $^{18}$F-Nifene: A measure of acetylcholine competition. *Synapse*, *61*, 29–36. https://doi.org/10.1002/syn.20338

Fodero, L. R., Sáez-Valero, J., McLean, C. A., Martins, R. N., Beyreuther, K., Masters, C. L., Robertson, T. A., & Small, D. H. (2002). Altered glycosylation of acetylcholinesterase in APP (SW) Tg2576 transgenic mice occurs prior to amyloid plaque deposition. *Journal of Neurochemistry*, *81*(3), 441–448. https://doi.org/10.1046/j.1471-4159.2002.00902.x

Forner, S., Kawauchi, S., Balderrama-Gutierrez, G., Kramár, E. A., Matheos, D. P., Phan, J., Javonillo, D. I., Tran, K. M., Hingco, E., da Cunha, C., Rezaie, N., Alcantara, J. A., Baglietto-Vargas, D., Jansen, C., Neumann, J., Wood, M. A., MacGregor, G. R., Mortazavi, A., Tenner, A. J., … Green, K. N. (2021). Systematic phenotyping and characterization of the 5xFAD mouse model of Alzheimer's disease. *Scientific Data*, *8*, 270.

Franke, T. N., Irwin, C., Bayer, T. A., Brenner, W., Beindorff, N., Bouter, C., & Bouter, Y. (2020). *In vivo* imaging with $^{18}$F-FDG- and $^{18}$F-Florbetaben-PET/MRI detects pathological changes in the brain of the commonly used 5XFAD mouse model of Alzheimer's disease. *Frontiers in Medicine*, *7*, 529. https://doi.org/10.3389/fmed.2020.00529

Frost, G. R., Longo, V., Li, T., Jonas, L. A., Judenhofer, M., Cherry, S., Koutcher, J., Lekaye, C., Zanzonico, P., & Li, Y. M. (2020). Hybrid PET/MRI enables high-spatial resolution, quantitative imaging of amyloid plaques in an Alzheimer's disease mouse model. *Scientific Reports*, *10*(1), 13826. https://doi.org/10.1038/s41598-020-70134-7

German, D. C., Yazdani, U., Speciale, S. G., Pasbakhsh, P., Games, D., & Liang, C. L. (2003). Cholinergic neuropathology in a mouse model of Alzheimer's disease. *The Journal of Comparative Neurology*, *462*(4), 371–381. https://doi.org/10.1002/cne.10737

Gori, S., Inno, A., Lunardi, G., Gorgoni, G., Malfatti, V., Severi, F., Alongi, F., Carbognin, G., Romano, L., Pasetto, S., & Salgarello, M. (2015). 18F-sodium fluoride PET-CT for the assessment of brain metastasis from lung adenocarcinoma. *Journal of Thoracic Surgery*, *10*(8), e67–e68. https://doi.org/10.1097/JTO.0000000000000523

Hillmer, A. T., Wooten, D. W., Moirano, J. M., Slesarev, M., Barnhart, T. E., Engle, J. W., Nickles, R. J., Murali, D., Schneider, M. L., Mukherjee, J., & Christian, B. T. (2011). Specific $\alpha4\beta2$ nicotinic acetylcholine receptor binding of [F-18]nifene in the rhesus monkey. *Synapse*, *65*(12), 1309–1318. https://doi.org/10.1002/syn.20965

Jullienne, A., Trinh, M. V., & Obenaus, A. (2022). Neuroimaging of mouse models of Alzheimer's disease. *Biomedicines*, *10*(2), 305. https://doi.org/10.3390/biomedicines10020305

Kamigaki, T. (2019). Prefrontal circuit organization for executive control. *Neuroscience Research*, *140*, 23–36. https://doi.org/10.1016/j.neures.2018.08.017

Kant, R., Constantinescu, C. C., Parekh, P., Pandey, S. K., Pan, M. L., Easwaramoorthy, B., & Mukherjee, J. (2011). Evaluation of F-nifene binding to $\alpha4\beta2$ nicotinic receptors in the rat brain using microPET imaging. *EJNMMI Research*, *1*, 6. https://doi.org/10.1186/2191-219X-1-6

Kaur, H., Felix, M. R., Liang, C., & Mukherjee, J. (2021). Development and evaluation of [$^{18}$F]Flotaza for a$\beta$ plaque imaging in postmortem human Alzheimer's disease brain. *Bioorganic & Medicinal Chemistry Letters*, *46*, 128164. https://doi.org/10.1016/j.bmcl.2021.128164

Kawarabayashi, T., Younkin, L. H., Saido, T. C., Shoji, M., Ashe, K. H., & Younkin, S. G. (2001). Age-dependent changes in brain, CSF, and plasma amyloid (beta) protein in the Tg2576 transgenic mouse model of Alzheimer's disease. *The Journal of Neuroscience*, *21*(2), 372–381. https://doi.org/10.1523/JNEUROSCI.21-02-00372.2001

Koukouli, F., Rooy, M., Changeux, J. P., & Maskos, U. (2016). Nicotinic receptors in mouse prefrontal cortex modulate ultraslow fluctuations related to conscious processing. *Proceedings of the National Academy of Sciences of the United States of America*, *113*(51), 14823–14828. https://doi.org/10.1073/pnas.1614417113

Koveri, E., Charidimou, A., Herrman, F. R., Giannakopoulos, P., Bouras, C., & Gold, G. (2015). No neuropathological evidence for a direct topographical relation between microbleeds and cerebral amyloid angiopathy. *Acta Neuropathologica Communications*, *3*, 49.

Lombardo, S., & Maskos, U. (2015). Role of the nicotinic acetylcholine receptor in Alzheimer's disease pathology and treatment. *Neuropharmacology*, *96*(Pt B), 255–262. https://doi.org/10.1016/j.neuropharm.2014.11.018

Luo, F., Rustay, N. R., Ebert, U., Hradil, V. P., Cole, T. B., Llano, D. A., Mudd, S. R., Zhang, Y., Fox, G. B., & Day, M. (2012). Characterization of 7- and 19-month-old Tg2576 mice using multimodal in vivo imaging: Limitations as a translatable model of Alzheimer's disease. *Neurobiology of Aging*, *33*(5), 933–944. https://doi.org/10.1016/j.neurobiolaging.2010.08.005

Ma, Y., Smith, D., Hof, P. R., Foerster, B., Hamilton, S., Blackband, S. J., Yu, M., & Benveniste, H. (2008). In vivo 3D digital atlas database of the adult C57BL/6J mouse brain by magnetic resonance microscopy. *Frontiers in Neuroanatomy*, *2*, 1. https://doi.org/10.3389/neuro.05.001.2008

Macdonald, I. R., DeBay, D. R., Reid, G. A., O'Leary, T. P., Jollymore, C. T., Mawko, G., Burrell, S., Martin, E., Bowen, C. V., Brown, R. E., & Darvesh, S. (2014). Early detection of cerebral glucose uptake changes in the 5XFAD mouse. *Current Alzheimer Research*, *11*(5), 450–460. https://doi.org/10.2174/1567205011666140505111354

Martín, A., Szczupak, B., Gómez-Vallejo, V., Domercq, M., Cano, A., Padro, D., Muñoz, C., Higuchi, M., Matute, C., & Llop, J. (2015). In vivo PET imaging of the $\alpha4\beta2$ nicotinic acetylcholine receptor as a marker for brain inflammation after cerebral ischemia. *The Journal of Neuroscience*, *35*(15), 5998–6009. https://doi.org/10.1523/JNEUROSCI.3670-14.2015

Marucci, G., Buccioni, M., Ben, D. D., Lambertucci, C., Volpini, R., & Amenta, F. (2021). Efficacy of acetylcholinesterase inhibitors in Alzheimer's disease. *Neuropharmacology*, *190*, 108352. https://doi.org/10.1016/j.neuropharm.2020.108352

Marutle, A., Warpman, U., Bogdanovic, N., Lannfelt, L., & Nordberg, A. (1999). Neuronal nicotinic receptor deficits in Alzheimer patients with the Swedish amyloid precursor protein 670/671 mutation. *Journal of Neurochemistry*, *72*(3), 1161–1169. https://doi.org/10.1046/j.1471-4159.2000.0721161.x

Mirzaei, N., Tang, S. P., Ashworth, S., Coello, C., Plisson, C., Passchier, J., Selvaraj, V., Tyacke, R. J., Nutt, D. J., & Sastre, M. (2016). In vivo imaging of microglial activation by positron emission tomography with [(11)C]PBR28 in the 5XFAD model of Alzheimer's disease. *Glia*, *64*(6), 993–1006. https://doi.org/10.1002/glia.22978

Mitsis, E. M., Reech, K. M., Bois, F., Tamagnan, G. D., Macavoy, M. G., Seibyl, J. P., Staley, J. K., & van Dyck, C. H. (2009). 123I-5-IA-85380 SPECT imaging of nicotinic receptors in Alzheimer disease and mild cognitive impairment. *Journal of Nuclear Medicine*, *50*(9), 1455–1463. https://doi.org/10.2967/jnumed.109.064030

Mondal, R., Campoy, A. T., Liang, C., & Mukherjee, J. (2021). [$^{18}$ F]FDG PET/CT studies in transgenic Hualpha-Syn (A53T) Parkinson's disease mouse model of $\alpha$-Synucleinopathy. *Frontiers in Neuroscience*, *15*, 676257. https://doi.org/10.3389/fnins.2021.676257

Mukherjee, J., Ladwa, R. M., Liang, C., & Syed, A. U. (2022). Elevated monoamine oxidase-A in anterior cingulate of postmortem human Parkinson's disease: A potential surrogate biomarker for Lewy bodies? *Cells*, *11*(24), 4000. https://www.mdpi.com/2073-4409/11/24/4000

Mukherjee, J., Lao, P. J., Betthauser, T. J., Samra, G. K., Pan, M. L., Patel, I. H., Liang, C., Metherate, R., & Christian, B. T. (2018). Human brain imaging of nicotinic acetylcholine $\alpha4\beta2^*$ receptors using [$^{18}$ F]Nifene: Selectivity, functional activity, toxicity, aging effects, gender effects, and extrathalamic pathways. *The Journal of Comparative Neurology*, *526*(1), 80–95. https://doi.org/10.1002/cne.24320

Mukherjee, J., Liang, C., Campoy, A., Kaur, H., Syed, A. U., & Danh, T. B. (2021). Human hippocampal [$^{18}$F]nifene binding to nicotinic acetylcholinergic $\alpha4\beta2^*$ receptors is reduced in postmortem Alzheimer's disease brains. *Journal of Cerebral Blood Flow Metabolism*, *41*(1), 146–147.

Nguyen, G., Liang, C., & Mukherjee, J. (2022). [$^{124}$I]IBETA: A new a$\beta$ plaque positron emission tomography imaging agent for Alzheimer's disease. *Molecules*, *27*(14), 4552. https://doi.org/10.3390/molecules27144552

Nordberg, A. (1994). Human nicotinic receptors—Their role in aging and dementia. *Neurochemistry International*, *25*(1), 93–97. https://doi.org/10.1016/0197-0186(94)90059-0

Oakley, H., Cole, S. L., Logan, S., Maus, E., Shao, P., Craft, J., Guillozet-Bongaarts, A., Ohno, M., Disterhoft, J., Van Eldik, L., & Berry, R. (2006). Intraneuronal $\beta$-amyloid aggregates, neurodegeneration, and neuron loss in transgenic mice with five familial Alzheimer's disease mutations: Potential factors in amyloid plaque formation. *Journal of Neuroscience*, *26*(40), 10129–10140.

Oblak, A. L., Lin, P. B., Kotredes, K. P., Pandey, R. S., Garceau, D., Williams, H. M., Uyar, A., O'Rourke, R., O'Rourke, S., Ingraham, C., Bednarczyk, D., Belanger, M., Cope, Z. A., Little, G. J., Williams, S. G., Ash, C., Bleckert, A., Ragan, T., Logsdon, B. A., … Lamb, B. T. (2021). Comprehensive evaluation of the 5XFAD mouse model for preclinical testing applications: A MODEL-AD study. *Frontiers in Aging Neuroscience*, *13*, 713726. https://doi.org/10.3389/fnagi.2021.713726

Okada, H., Ouchi, Y., Ogawa, M., Futatsubashi, M., Saito, Y., Yoshikawa, E., Terada, T., Oboshi, Y., Tsukada, H., Ueki, T., Watanabe, M., Yamashita, T., & Magata, Y. (2013). Alterations in $\alpha4\beta2$ nicotinic receptors in cognitive decline in Alzheimer's aetiopathology. *Brain*, *136*(Pt 10), 3004–3017. https://doi.org/10.1093/brain/awt195

Ono, M., Cheng, Y., Kimura, H., Watanabe, H., Matsumura, K., Yoshimura, M., Iikuni, S., Okamoto, Y., Ihara, M., Takahashi, R., & Saji, H. (2013). Development of novel 123I-labeled pyridyl benzofuran derivatives for SPECT imaging of $\beta$-amyloid plaques in Alzheimer's disease. *PLoS One*, *8*(9), e74104. https://doi.org/10.1371/journal.pone.0074104

Pan, M. L., Mukherjee, M. T., Patel, H. H., Patel, B., Constantinescu, C. C., Mirbolooki, M. R., Liang, C., & Mukherjee, J. (2016). Evaluation of [11C]TAZA for amyloid $\beta$ plaque imaging in postmortem human Alzheimer's disease brain region and whole body distribution in rodent PET/CT. *Synapse*, *70*(4), 163–176. https://doi.org/10.1002/syn.21893

Pichika, R., Easwaramoorthy, B., Collins, D., Christian, B. T., Shi, B., Narayanan, T. K., Potkin, S. G., & Mukherjee, J. (2006). Nicotinic alpha4beta2 receptor imaging agents: Part II. Synthesis and biological evaluation of 2-[18F]fluoro-3-[2-((S)-3-pyrrolinyl)methoxy]pyridine (18F-nifene) in rodents and imaging by PET in nonhuman primate. *Nuclear Medicine and Biology*, *33*(3), 295–304. https://doi.org/10.1016/j.nucmedbio.2005.12.017

Premachandran, H., Zhao, M., & Arruda-Carvalho, M. (2020). Sex differences in the development of the rodent corticolimbic system. *Frontiers in Neuroscience*, *14*, 583477. https://doi.org/10.3389/fnins.2020.583477

Rees, T., Hammond, P. I., Soreq, H., Younkin, S., & Brimijoin, S. (2003). Acetylcholinesterase promotes beta-amyloid plaques in cerebral cortex. *Neurobiology of Aging*, *24*(6), 777–787. https://doi.org/10.1016/s0197-4580(02)00230-0

Rejc, L., Gomez-Vallejo, V., Joya, A., Arsequell, G., Egimendia, A., Castellnou, P., Rios-Anglada, X., Cossio, U., Baz, Z., Iglesias, L., Capetillo-Zarate, E., Ramos-Cabrer, P., Martin, A., & Llop, J. (2022). Longitudinal evaluation of neuroinflammation and oxidative stress in a mouse model of Alzheimer disease using positron emission tomography. *Alzheimer's Research & Therapy*, *14*, 80.

Sabri, O., Meyer, P. M., Gräf, S., Hesse, S., Wilke, S., Becker, G. A., Rullmann, M., Patt, M., Luthardt, J., Wagenknecht, G., Hoepping, A., Smits, R., Franke, A., Sattler, B., Tiepolt, S., Fischer, S., Deuther-Conrad, W., Hegerl, U., Barthel, H., … Brust, P. (2018). Cognitive correlates of $\alpha4\beta2$ nicotinic acetylcholine receptors in mild Alzheimer's dementia. *Brain*, *141*(6), 1840–1854. https://doi.org/10.1093/brain/awy099

Salloway, S., Sperling, R., Fox, N. C., Blennow, K., Klunk, W., Raskind, M., Sabbagh, M., Honig, L. S., Porsteinsson, A. P., Ferris, S., Reichert, M., Ketter, N., Nejadnik, B., Guenzler, V., Miloslavsky, M., Wang, D., Lu, Y., Lull, J., Tudor, I. C., Bapineuzumab 301 and 302 Clinical Trial Investigators. (2014). Two phase 3 trials of bapineuzumab in mild-to-moderate Alzheimer's disease. *The New England Journal of Medicine*, *370*(4), 322–333. https://doi.org/10.1056/NEJMoa1304839

Samra, G. K., Dang, K., Ho, H., Baranwal, A., & Mukherjee, J. (2018). Dual targeting agents for a$\beta$ plaque/P-glycoprotein and a$\beta$ plaque/nicotinic acetylcholine $\alpha4\beta2^*$ receptors-potential approaches to facilitate a$\beta$ plaque removal in Alzheimer's disease brain. *Medicinal Chemistry Research*, *27*(6), 1634–1646. https://doi.org/10.1007/s00044-018-2178-9

Shih, A. Y., Hyacinth, H. I., Hartmann, D. A., & van Veluw, S. J. (2018). Rodent models of cerebral microinfarct and microhemorrhage. *Stroke; A Journal of Cerebral Circulation*, *49*(3), 803–810. https://doi.org/10.1161/STROKEAHA.117.016995

Sultzer, D. L., Lim, A. C., Gordon, H. L., Yarns, B. C., & Melrose, R. J. (2022). Cholinergic receptor binding in unimpaired older adults, mild cognitive impairment, and Alzheimer's disease dementia. *Alzheimer's Research & Therapy*, *14*(1), 25. https://doi.org/10.1186/s13195-021-00954-w

Sultzer, D. L., Melrose, R. J., Riskin-Jones, H., Narvaez, T. A., Veliz, J., Ando, T. K., Juarez, K. O., Harwood, D. G., Brody, A. L., & Mandelkern, M. A. (2017). Cholinergic receptor binding in Alzheimer disease and healthy aging: Assessment in vivo with positron emission tomography imaging. *The American Journal of Geriatric Psychiatry*, *25*(4), 342–353. https://doi.org/10.1016/j.jagp.2016.11.011

van Heukelum, S., Mars, R. B., Guthrie, M., Buitelaar, J. K., Beckmann, C. F., Tiesinga, P., Vogt, B. A., Glennon, J. C., & Havenith, M. N. (2020). Where is cingulate cortex? A cross-species view. *Trends in Neurosciences*, *43*(5), 285–299. https://doi.org/10.1016/j.tins.2020.03.007

Vignal, N., Cisternino, S., Rizzo-Padoin, N., San, C., Hontonnou, F., Gelé, T., Declèves, X., Sarda-Mantel, L., & Hosten, B. (2018). [$^{18}$F]FEPPA a TSPO radioligand: Optimized radiosynthesis and evaluation as a PET radiotracer for brain inflammation in a peripheral LPS-Injected mouse model. *Molecules (Basel, Switzerland)*, *23*(6), 1375. https://doi.org/10.3390/molecules23061375

Webster, S. J., Bachstetter, A. D., Nelson, P. T., Schmitt, F. A., & Van Eldik, L. J. (2014). Using mice to model Alzheimer's dementia: An overview of the clinical disease and the preclinical behavioral changes in 10 mouse models. *Frontiers in Genetics*, *5*, 88. https://doi.org/10.3389/fgene.2014.00088

Wengenack, T. M., Reyes, D. A., Curran, G. L., Borowski, B. J., Lin, J., Preboske, G. M., Holasek, S. S., Gilles, E. J., Chamberlain, R., Marjanska, M., Jack, C. R., Garwood Jr, M., & Poduslo, J. F. (2011). Regional differences in MRI detection of amyloid plaques in AD transgenic mouse brain. *Neuroimage*, *54*(1), 113–122. https://doi.org/10.1016/j.neuroimage.2010.08.033

Wu, J., Kuo, Y. P., George, A. A., Xu, L., Hu, J., & Lukas, R. J. (2004). beta-Amyloid directly inhibits human alpha4beta2-nicotinic acetylcholine receptors heterologously expressed in human SH-EP1 cells. *The Journal of Biological Chemistry*, *279*(36), 37842–37851. https://doi.org/10.1074/jbc.M400335200

Yin, X., Zhang, X., Zhang, J., Yang, W., Sun, X., Zhang, H., Gao, Z., & Jiang, H. (2022). High-Resolution digital panorama of multiple structures in whole brain of Alzheimer's disease mice. *Frontiers in Neuroscience*, *16*, 870520. https://doi.org/10.3389/fnins.2022.870520

Zhang, H. J., Zammit, M., Kao, C., Govind, A., Mitchell, S., Holderman, N., Bhuiyan, M., Freifelder, R., Zhuang, X., Mukherjee, J., Chen, C. T., & Green, W. N. (2022). Trapping of nicotinic acetylcholine receptor ligands assayed by in vitro cellular studies and in vivo PET imaging. *Journal of Neuroscience*, *43*(1), 2–13. https://doi.org/10.1523/JNEUROSCI.2484-21.2022

Zuin, M., Cherubini, A., Volpato, S., Ferrucci, L., & Zuliani, G. (2022). Acetyl-cholinesterase-inhibitors slow cognitive decline and decrease overall mortality in older patients with dementia. *Scientific Reports*, *12*(1), 12214. https://doi.org/10.1038/s41598-022-16476-w

**How to cite this article:** Liang, C., Nguyen, G. A., Danh, T. B., Sandhu, A. K., Melkonyan, L. L., Syed, A. U., & Mukherjee, J. (2023). Abnormal [$^{18}$F]NIFENE binding in transgenic 5xFAD mouse model of Alzheimer's disease: In vivo PET/CT imaging studies of $\alpha 4\beta 2^*$ nicotinic acetylcholinergic receptors and in vitro correlations with A$\beta$ plaques. *Synapse*, 1–20. https://doi.org/10.1002/syn.22265